Published for SISSA by Springer

Received: April 25, 2024
Revised: July 15, 2024
Accepted: July 23, 2024
Published: August 27, 2024

Study of the electromagnetic form factors of the nucleons in the timelike region

Qin-He Yang,[a,b] **Di Guo,**[a,c] **Ming-Yan Li,**[a,c] **Ling-Yun Dai**[a,c,*] **Johann Haidenbauer**[d] **and Ulf-G. Meißner**[b,d,e]

[a] *School for Theoretical Physics, School of Physics and Electronics, Hunan University, Changsha 410082, China*
[b] *Helmholtz Institut für Strahlen- und Kernphysik and Bethe Center for Theoretical Physics, Universität Bonn, D-53115 Bonn, Germany*
[c] *Hunan Provincial Key Laboratory of High-Energy Scale Physics and Applications, Hunan University, Changsha 410082, China*
[d] *Institute for Advanced Simulation (IAS-4), Forschungszentrum Jülich, D-52425 Jülich, Germany*
[e] *Tbilisi State University, Tbilisi 0186, Georgia*

E-mail: yqh@hnu.edu.cn, diguo@hnu.edu.cn, 20000621@hnu.edu.cn, dailingyun@hnu.edu.cn, j.haidenbauer@fz-juelich.de, meissner@hiskp.uni-bonn.de

Abstract: The electromagnetic form factors $G_{\rm E}$ and $G_{\rm M}$ of the proton and neutron in the timelike region are extracted in a study of the processes $e^+e^- \to \bar{p}p$ and $e^+e^- \to \bar{n}n$. The reaction amplitude is evaluated within the distorted wave Born approximation, with the interaction of the antinucleon-nucleon ($\bar{N}N$) pair taken into account. The latter is constructed within SU(3) chiral effective field theory up to next-to-leading order. An excellent description of the $e^+e^- \to \bar{N}N$ data in the energy region from the $\bar{N}N$ threshold up to center-of-mass energies $E_{\rm cm} = 2.2\,\text{GeV}$ is achieved. Results for the electromagnetic form factors $G_{\rm E}, G_{\rm M}$, $G_{\rm E}/G_{\rm M}$, and the subtracted effective form factors, $G_{\rm osc}$, are provided. These can be helpful for further studies of the properties of the nucleons.

Keywords: Chiral Lagrangian, Properties of Hadrons

ArXiv ePrint: 2404.12448

*Corresponding author.

https://doi.org/10.1007/JHEP08(2024)208

Contents

1 Introduction

The nucleons and their properties are of fundamental interest in nuclear and particle physics as they are the basic components of nuclei, which constitute common matter. The electromagnetic form factors (EMFFs) of the proton and the neutron play an important role in understanding the properties of the internal structure of nucleons as well as strong interactions, see, e.g., refs. [1, 2] for reviews on recent progress. Indeed, the amplitudes of $eN \to eN$, $e^+e^- \to \bar{N}N$ and $\bar{N}N \to e^+e^-$ can be written in terms of the electric and magnetic form factors: $G_{\rm E}$ and $G_{\rm M}$, i.e., the so-called EMFFs. The EMFFs in the timelike region have recently received considerable attention from the physics community [3–12]. They can be studied through the annihilation of positron-electron into antinucleon-nucleon pairs and/or the inverse processes.

In the early stages, in the 1970s, the reaction $e^+e^- \to \bar{p}p$ was measured at center-of-mass energies $E_{\rm cm} = 2.1\,\text{GeV}$ and the EMFFs of the proton were extracted in an experiment at ADONE [13]. Subsequently, several measurements of the proton EMFFs were performed by other experimental groups, see, e.g., refs. [14–19]. The study of proton EMFFs also benefitted from measurements on $\bar{p}p$ annihilating into e^+e^- pairs [20]. On the other hand,

JHEP08(2024)208

measurements of neutron EMFFs are rather sparse. The Fenice collaboration studied the EMFFs in the process $e^+e^- \to \bar{n}n$ [17, 19]. Although those measurements launched a new era of this interesting field, they had limited statistics and a limited energy range. Fortunately, the situation has improved significantly in the 21st century. The BaBar, CMD-3, BESIII, and SND collaborations have performed various measurements of the EMFFs, and the uncertainties are now much smaller. See e.g., refs. [21–29] for the proton EMFFs, and refs. [30–34] for those of the neutron. Interestingly, the improved measurements suggested an apparent oscillatory behavior of the proton EMFFs. This aspect was first conjectured based on the measurements of the BaBar collaboration [21, 22] and reported in ref. [3]. The latest measurements of $e^+e^- \to \bar{p}p$ [29] and $e^+e^- \to \bar{n}n$ [32] by the BESIII collaboration established that also the neutron EMFFs show an oscillatory behavior. Moreover, and intriguingly, a phase difference in the oscillations of the EMFFs between the proton and the neutron has been found in the energy range of $E_{\rm cm} \in [2.00, 3.08]$ GeV [32]. This attracted further interest in timelike EMFFs, as it could be an important clue to reveal the internal structure and the interactions of nucleons. A natural question following the experimental result is whether this phenomenon holds true close to the threshold as well. Specifically, since the oscillation is observed in the effective EMFFs, does the phase difference still exists in the individual EMFFs of the nucleons? To answer these questions, one needs to study the EMFFs in the low energy region, that is, $E_{\rm cm} \in [2M_N, 2.2\ \text{GeV}]$, where M_N is the nucleon mass, and extract the individual EMFFs. This is the primary goal of this paper.

The situation around the $\bar{N}N$ threshold is still not clear, as it is not easy for experimentalists to perform measurements with sufficient statistics in this energy region. Nevertheless, the CMD-3 and SND collaborations published pertinent data on the cross sections for $e^+e^- \to \bar{p}p$ and $e^+e^- \to \bar{n}n$, respectively [24, 33]. Their measurements, though still afflicted by large errors, are helpful for further analysis of the EMFFs. On the theoretical side, investigations in the near-threshold region require the inclusion of the $\bar{N}N$ interaction in the final state in order to be conclusive. Indeed, it has been shown in several studies that the $\bar{N}N$ final-state interaction (FSI) has non-negligible effects around the threshold.[1] Since chiral effective field theory (χEFT) is successful in describing the interaction between baryons in the low-energy region [38, 39], we will adopt this framework to generate an appropriate hadronic $\bar{N}N$ scattering amplitude. Similar to what is done in our previous works and also by some other groups, we apply a two-step procedure to evaluate the reaction amplitude for $e^+e^- \to \bar{N}N$. The hadronic $\bar{N}N$ scattering amplitude is obtained by solving the Lippmann-Schwinger (LS) equation for an interaction potential derived within SU(3) χEFT. Then, the amplitude of e^+e^- annihilating into $\bar{N}N$ pairs is computed based on the distorted wave Born approximation (DWBA) [40–43]. This two-step procedure, combining χEFT and DWBA, as discussed above, has already been proven to be successful in studying the EMFFs, not only for nucleons but also for other baryons. See e.g., applications in the reactions $e^+e^- \leftrightarrow \bar{N}N$ [10, 40], $e^+e^- \to \bar{\Lambda}\Lambda$ [44, 45], $e^+e^- \to \Sigma^+\bar{\Sigma}^-$,... [42, 46], $e^+e^- \to \Lambda_c^+\bar{\Lambda}_c^-$ [41] and so on.

This paper is organized as follows: in section 2, we describe the calculation of the amplitude and cross section of the processes of $e^+e^- \to \bar{p}p$ and $e^+e^- \to \bar{n}n$, with the FSI in the $\bar{N}N$ system taken into account. In section 3, we present our fit to the phase shifts of

[1] For further discussions of FSI effects we refer to refs. [35–37].

JHEP08(2024)208

the coupled ${}^3S_1 - {}^3D_1$ partial wave in the isospin basis and the experimental data sets for $\bar{N}N$ cross sections and differential cross sections, in which the low-energy constants (LECs) of χEFT as well as other parameters are fixed. Then, the individual EMFFs of the proton and the neutron from the threshold up to 2.2 GeV are extracted, and the underlying physical interpretation is discussed. Finally, a brief summary is given in section 4. Details of the derivation of the $\bar{N}N$ interaction potential from SU(3) χEFT and various technicalities about loop integrals are compiled in appendices.

2 Theoretical framework

2.1 Formulas for the amplitude of $e^+e^- \to \bar{N}N$ and the EMFFs

In the assumption of one photon exchange, i.e., the electron-positron will annihilate into a virtual photon before hadronization, the differential cross section can be calculated from the helicity amplitudes ϕ_i for the scattering of two spin-1/2 particles [40]

$$\frac{\mathrm{d}\sigma}{\mathrm{d}\Omega} = \frac{1}{2s}\beta\, C(s) \sum_{i=1}^{8} |\phi_i|^2 \,, \tag{2.1}$$

where β is the phase space factor, $\beta = k_N/k_e$ with k_N, k_e the three-momenta of the nucleon and electron in the center-of-mass frame (c.m.f.). The momenta are related to the total energy by $\sqrt{s} = 2\sqrt{M_N^2 + k_N^2} = 2\sqrt{m_e^2 + k_e^2}$, with $m_e(M_N)$ the electron (nucleon) mass. $C(s)$ is the S-wave Sommerfeld-Gamow factor, $C(y) = y/(1 - e^{-y})$ with $y = \pi\alpha M_N/k_N$, where $\alpha = 1/137.036$ is the fine-structure constant. For neutrons $C(y) \equiv 1$. The ϕ_i are related to the angular momentum helicity states

$$\langle \lambda_1' \lambda_2' | F | \lambda_1 \lambda_2 \rangle = \sum_J (2J+1) \langle \lambda_1' \lambda_2' | F^J | \lambda_1 \lambda_2 \rangle d^J_{\lambda\lambda'}(\theta) \,, \tag{2.2}$$

with $\lambda_{1,2}^{(\prime)} = \pm\frac{1}{2}$, $\lambda^{(\prime)} = \lambda_1^{(\prime)} - \lambda_2^{(\prime)}$ and $d^J_{\lambda\lambda'}(\theta)$ the Wigner d-functions. To implement the information of the partial waves from χEFT, one needs to specify the quantum numbers. The transformation of the amplitudes from the helicity basis $|JM\lambda_1^{(\prime)}\lambda_2^{(\prime)}\rangle$ to the usual partial wave representation, $|JMLS\rangle$, is given by [47, 48],

$$\begin{aligned}\langle \lambda_1' \lambda_2' | F^J | \lambda_1 \lambda_2 \rangle = \sum_{LS,L'S'} & \frac{\sqrt{(2L+1)(2L'+1)}}{2J+1} \langle LS0\lambda | J\lambda \rangle \langle J\lambda' | L'S'0\lambda' \rangle \\ & \times \langle s_1 s_2 \lambda_1, -\lambda_2 | S\lambda \rangle \langle S'\lambda' | s_1' s_2' \lambda_1', -\lambda_2' \rangle \langle L'S'J | F | LSJ \rangle \,. \end{aligned} \tag{2.3}$$

In our analysis of $e^+e^- \to \bar{N}N$ the situation is simple because one only needs to deal with the ${}^3S_1 - {}^3D_1$ partial waves.[2] The helicity amplitudes are decomposed into [40, 49, 50]

$$\begin{aligned}
\phi_1 &= \langle ++|F|++\rangle = \frac{\cos\theta}{2}[F_{00} - \sqrt{2}(F_{02} + F_{20}) + 2F_{22}] = -\frac{2m_e M_N \alpha}{s}\cos\theta G_{\mathrm{E}}^N \,, \\
\phi_2 &= \langle ++|F|--\rangle = \phi_1 \,, \\
\phi_3 &= \langle +-|F|+-\rangle = \frac{1+\cos\theta}{4}[F_{22} + 2F_{00} + \sqrt{2}(F_{02} + F_{20})] = -\frac{\alpha}{2}(1+\cos\theta) G_{\mathrm{M}}^N \,,
\end{aligned}$$

[2] The amplitude written in eq. (2.4) is valid for one-photon exchange. Higher order terms of the electromagnetic vertex are neglected. Conservation of parity, charge conjugation, and time reversal invariance have been taken into account.

JHEP08(2024)208

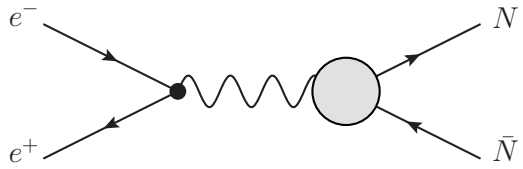

Figure 1. Illustrative diagram of the process $e^+e^- \to \bar{N}N$.

$$
\begin{aligned}
\phi_4 &= \langle +- |F| -+ \rangle = \frac{1-\cos\theta}{4}[F_{22} + 2F_{00} + \sqrt{2}(F_{02} + F_{20})] = -\frac{\alpha}{2}(1-\cos\theta)G_{\rm M}^N\,, \\
\phi_5 &= \langle ++ |F| +- \rangle = -\frac{\sin\theta}{2\sqrt{2}}[F_{02} - 2F_{20} - \sqrt{2}(F_{22} - F_{00})] = \frac{M_N\alpha}{\sqrt{s}}\sin\theta G_{\rm E}^N\,, \\
\phi_6 &= \langle +- |F| ++ \rangle = \frac{\sin\theta}{2\sqrt{2}}[F_{20} - 2F_{02} - \sqrt{2}(F_{22} - F_{00})] = -\frac{m_e\alpha}{\sqrt{s}}\sin\theta G_{\rm M}^N\,, \\
\phi_7 &= \langle ++ |F| -+ \rangle = -\phi_5\,, \\
\phi_8 &= \langle -+ |F| ++ \rangle = -\phi_6\,.
\end{aligned}
\tag{2.4}
$$

Here, $F_{L'L}$ is the partial wave amplitude of the process $e^+e^- \to \bar{N}N$, as shown in figure 1. It can be written as a product of two factors: one is the $e^+e^-\gamma$ vertex, and the other is the $\bar{N}N\gamma$ effective vertex. Accordingly, the amplitude factorizes into

$$
F_{LL'}^{\bar{N}N,e^+e^-} = -\frac{4\alpha}{9} f_L^{\bar{N}N} f_{L'}^{e^+e^-}\,,
$$

with

$$
\begin{aligned}
f_0^{\bar{N}N} &= G_{\rm M}^N + \frac{M_N}{\sqrt{s}}G_{\rm E}^N\,, & f_0^{e^+e^-} &= 1 + \frac{m_e}{\sqrt{s}}\,, \\
f_2^{\bar{N}N} &= \frac{1}{\sqrt{2}}\left(G_{\rm M}^N - \frac{2M_N}{\sqrt{s}}G_{\rm E}^N\right)\,, & f_2^{e^+e^-} &= \frac{1}{\sqrt{2}}\left(1 - \frac{2m_e}{\sqrt{s}}\right)\,.
\end{aligned}
\tag{2.5}
$$

Obviously, one has $G_{\rm E}^N = G_{\rm M}^N$ at the $\bar{N}N$ thresholds which follows from the definition of the Sachs form factors. Once the production amplitude has been obtained, one can obtain the individual EMFFs by eq. (2.5).

2.2 Implementation of the $\bar{N}N$ FSI

As has been mentioned in the context of eq. (2.5), the vertex $\bar{N}N\gamma$ should include the FSI in the $\bar{N}N$ system. In the present work this is realized within the DWBA [40, 41]:

$$
f_L^{\bar{N}N}(k_N; E_{k_N}) = f_L^{\bar{N}N,0}(k_N) + \sum_{L'}\int_0^\infty \frac{{\rm d}pp^2}{(2\pi)^3} f_{L'}^{\bar{N}N,0}(p)\frac{1}{2E_{k_N} - 2E_p + i0^+}T_{L'L}(p, k_N; E_{k_N})\,.
\tag{2.6}
$$

A diagrammatic representation of eq. (2.6) can be found in figure 2, where the full $\bar{N}N\gamma$ vertex is represented by the large shaded circle, while the first diagram on the right-hand side is the so-called Born term, representing the bare $\bar{N}N\gamma$ production vertex $f_L^{\bar{N}N,0}$. We introduce two parameters to be fixed by fitting to the available experiments: $G_{\rm E}^{\bar{p}p,0} = G_{\rm M}^{\bar{p}p,0}$

JHEP08(2024)208

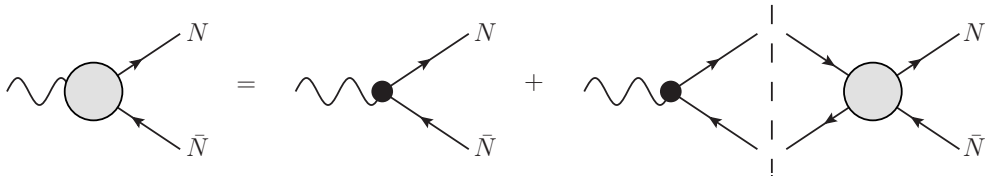

Figure 2. Diagrammatic representation of the vertex $\bar{N}N\gamma$ ($\gamma \to \bar{N}N$) consisting of the Born term and re-scattering in the $\bar{N}N$ system.

and $G_{\rm E}^{\bar{n}n,0} = G_{\rm M}^{\bar{n}n,0}$, with

$$f_0^{\bar{N}N,0}(p) = G_{\rm M}^{\bar{N}N,0} + \frac{M_N}{2\sqrt{M_N^2+p^2}} G_{\rm E}^{\bar{N}N,0}, \quad f_2^{\bar{N}N,0}(p) = \frac{1}{\sqrt{2}} \left(G_{\rm M}^{\bar{N}N,0} - \frac{M_N}{\sqrt{M_N^2+p^2}} G_{\rm E}^{\bar{N}N,0} \right) .$$

It should be stressed that the parameters $G_{\rm E/M}^{\bar{N}N,0}$ are complex due to possible intermediate annihilation processes, e.g., $\gamma \to \pi^+\pi^- \to \bar{N}N$. The second diagram on the right hand side in figure 2, corresponding to the integral part of eq. (2.6), provides the dressing of the vertex via $\bar{N}N$ re-scattering.

The $\bar{N}N$ scattering amplitude $T_{LL'}(p, k_N; E_{k_N})$ in the relevant coupled ${}^3S_1 - {}^3D_1$ partial wave will be calculated within the framework of SU(3) χEFT. Indeed, there are many studies of the baryon-baryon and/or baryon-antibaryon interactions based on χEFT. See e.g., refs. [38, 51–53] who derived the NN potential up to next-to-next-to-next-to-leading order (N^{3}LO) from SU(2) χEFT, and refs. [54–58] for the nucleon-nucleon (NN), hyperon-nucleon (YN), and hyperon-hyperon (YY) interaction potentials up to next-to-leading order (NLO) from SU(3) χEFT. The merit of the present analysis based on SU(3) χEFT is that the possible effects from kaon and η exchanges are included. This should be crucial since we want to study the EMFFs up to 2.2 GeV, i.e. up to energies close to the $\bar{\Lambda}\Lambda$ threshold. Note that in the energy region of $2 - 2.2$ GeV, there is a wealth of electromagnetic data on the reactions of $e^+e^- \to \bar{p}p$ and $e^+e^- \to \bar{n}n$, including some essential observables such as differential cross sections that help to fix the partial waves.

By exploiting the G-parity transformation the $\bar{N}N$ interaction can be easily derived from available NN potentials, at least as far as the elastic part is concerned. For example, the $\bar{N}N$ potential up to N^{2}LO [59] utilizes the expressions for the NN interaction of ref. [38] as starting point and the N^{3}LO potential by Dai et al. [60] is based on the NN potential by Epelbaum et al. [51]. Indeed, for the interaction due to one-boson exchange (OBE), G-parity implies simply that

$$V_{\bar{N}N}^{\rm OBE} = (-1)^I V_{NN}^{\rm OBE}, \tag{2.7}$$

where I is the isospin of the exchanged pseudoscalar meson. Also the contributions of two-boson exchange (TBE) involving pions and/or etas can be obtained through the G-parity transformation. However, it is not applicable for contributions involving the K and $\bar{K}$ mesons because these do not have a well defined G-parity. In that case a separate calculation is necessary, see appendix A. Once the $\bar{N}N$ potential is established we insert it into the LS equation to obtain the scattering amplitude [59, 61],

$$T_{L''L'}(p'', p'; E_k) = V_{L''L'}(p'', p') + \sum_L \int \frac{{\rm d}pp^2}{(2\pi)^3} V_{L''L}(p'', p) \frac{1}{2E_k - 2E_p + i0^+} T_{LL'}(p, p'; E_k) \, . \tag{2.8}$$

Here, $E_k = \sqrt{s}/2$ and $V_{L''L}(p'', p')$ is the $\bar{N}N$ potential. The details of calculating the potentials up to NLO based on SU(3) χEFT are summarized in appendix A. In contrast to $\bar{N}N$ potentials constructed within SU(2) χEFT, our interactions include η exchange in the OBE potential and $\pi\eta$, $\eta\eta$ and $K\bar{K}$ exchanges in the TBE potential. Inserting $T_{L''L'}(p'', p'; E_k)$ into eq. (2.6), one can get the final amplitude for $e^+e^- \to \bar{N}N$.

3 Results and discussion

3.1 Fit procedure

The hadronic scattering amplitudes are taken as input in eq. (2.6) to evaluate the electron-positron annihilation amplitude within the DWBA approach. Note that the amplitudes $T_{LL'}$ of $\bar{N}N$ scattering and $f_L^{\bar{N}N,I}$ of the $\bar{N}N\gamma$ vertex are obtained in the isospin basis. To fit the $e^+e^- \to \bar{N}N$ data, one needs to transform these amplitudes to the physical basis,

$$f_L^{\bar{p}p} = \frac{1}{\sqrt{2}}\left(f_L^{\bar{N}N,I=0} - f_L^{\bar{N}N,I=1}\right), \quad f_L^{\bar{n}n} = \frac{1}{\sqrt{2}}\left(f_L^{\bar{N}N,I=0} + f_L^{\bar{N}N,I=1}\right). \tag{3.1}$$

In the isospin basis, we use $M_N = (M_p + M_n)/2$, while in the calculation of the observables, such as differential cross section and cross sections, we take the physical masses in the phase-space factors. Once the $e^+e^- \to \bar{N}N$ amplitudes are established the EMFFs $G_{\rm M}$ and $G_{\rm E}$ can be extracted through eq. (2.5).

To fix the LECs of χEFT and other unknown parameters such as $G_{\rm E,M}^{N,0}$, we perform a combined fit to two kinds of data sets: one of them is the S-matrix elements from a partial-wave analysis (PWA) of $\bar{N}N$ scattering [62] and $\bar{N}N$ scattering lengths from χEFT [59, 61]. The other set includes the cross sections, angular distributions, and EMFFs of the processes of $e^+e^- \to \bar{N}N$ as well as $\bar{N}N \to e^+e^-$. With regard to $\bar{N}N$ scattering we focus on energies not too far from the threshold, because here we expect that χEFT works reliably. Specifically, we consider the first three momenta of the PWA [62] which means the region $T_{\rm lab} \leq 50\,\text{MeV}$. Accordingly, in that region, but also for somewhat higher energies, the results for the $e^+e^- \to \bar{N}N$ observables are primarily determined by the properties of the $\bar{N}N$ interaction. Thus, at those low energies (the energy dependence of) the EMFFs are true predictions. However, with increasing energy and, in particular, in the upper region of the considered energy range the outcome of the fit is more and more dominated by the $e^+e^- \to \bar{N}N$ data themselves, simply because here those are the only data that enter the fitting procedure. Then the $\bar{N}N$ interaction serves as an effective and phenomenological tool for the adjustments needed to describe those data. The resulting $\bar{N}N$ amplitudes themselves are not expected to be the physical ones. There are 7 LECs in the $\bar{N}N$ interaction for each of the two isospin channels, see eqs. (A.36), (A.37). Since they are all real numbers it implies a total of 14 LECs for the analysis. There are two more parameters, related to the Born term of the EMFFs, namely $G_{\rm E/M}^{0(I=0)}$ and $G_{\rm E/M}^{0(I=1)}$. Keep in mind that the overall phase of the amplitude is not an observable. Thus, it can not be determined in fitting the data. Therefore, one of the couplings of the EMFFs can be fixed to be real. Here, $G_{\rm E/M}^{0(I=0)}$ is chosen to be real. In addition, there are 9 normalization factors to fit the number of events of the angular distributions, as the efficiencies are not known. Thus, there are 26 parameters to be determined in total. On the other hand, there are 722 data points used in the analysis, including 154 cross-section values [21–25, 27–33, 63], 477 points of differential cross sections, 7

JHEP08(2024)208

cross sections ratios ($\sigma(e^+e^- \to \bar{n}n)/\sigma(e^+e^- \to \bar{p}p)$), 44 individual EMFFs ($G_{\rm M}$ and $G_{\rm E}$ that are extracted from the experiments), 18 S-matrix elements (complex) from the $\bar{N}N$ PWA [62] and 2 $\bar{N}N$ scattering lengths (complex) [59, 61]. As will be discussed in the following subsections, the parameters can be fixed well due to the availability of a large data set.

3.2 Fit to the $\bar{N}N$ scattering amplitudes

For simplicity, we will discuss the fit results of $\bar{N}N$ scattering in this subsection and the ones for $e^+e^- \to \bar{N}N$ in the next subsection. The $\bar{N}N$ potentials are calculated within SU(3) χEFT up to NLO, in which there are 14 LECs corresponding to contact terms in the elastic and the annihilation parts. To fix these parameters we fit to the S-matrix elements obtained in a PWA of $\bar{N}N$ scattering data [62]. The phase shifts for the coupled $\bar{N}N$ partial wave ${}^3S_1 - {}^3D_1$ can be extracted from the S-matrix as follows

$$\begin{pmatrix} S_{00} & S_{02} \\ S_{20} & S_{22} \end{pmatrix} = \begin{pmatrix} \cos(2\epsilon_1)e^{i2\delta_0} & -i\sin(2\epsilon_1)e^{i(\delta_0+\delta_2)} \\ -i\sin(2\epsilon_1)e^{i(\delta_0+\delta_2)} & \cos(2\epsilon_1)e^{i2\delta_2} \end{pmatrix}, \tag{3.2}$$

where we adapt the convention of refs. [59, 61, 62]. The relation between the S-matrix and the on-shell reaction amplitude T is given as

$$S_{LL'}(k) = \delta_{LL'} - \frac{i}{8\pi^2} k E_k T_{LL'}(k, k; E_k). \tag{3.3}$$

The phase shifts $\delta_{0,2}$ are complex numbers due to the presence of annihilation, see e.g. refs. [61, 62]. Thus, we plot both the real and imaginary parts of the phase shifts. As mentioned above, we only fit our amplitudes in the low-energy region, up to $T_{\rm lab} = 50\,$MeV. The fit results are shown in figure 3, where the 'data' points are taken from ref. [62]. Notice that, though we fit to the S-matrix elements of the PWA [62], we plot the phase shifts and inelasticities to allow for an easy comparison with our previous works [59, 61], where likewise the phase shifts were shown. We apply the values Λ =750, 800, 850, 900, and 950 MeV to explore the influence of the cutoff on our results. Notice that $\Lambda = 850\,$MeV corresponds to the upper limit, $\sqrt{s} = 2.2\,$GeV of this analysis. As can be seen in figure 3, all the results with different cutoffs are consistent with the PWA [62] in the energy region of $T_{\rm lab} \leq 50\,$MeV, in general even over the larger energy region of $T_{\rm lab} \leq 100\,$MeV, except for those of the D-waves.

The values of the LECs for the LO and NLO potentials of our fits are listed in table 1, where we use the conventions of ref. [61], that is $\tilde{C}_{^{2I+1}\,^{2S+1}L_J}$ and $C_{^{2I+1}\,^{2S+1}L_J}$, with the first superscript related to the isospin. Also, the other couplings, such as $G_{\rm E/M}^{0(I)}$ and the normalization factors for the event distribution data sets, are given, as they are fixed in the global fit. As can be observed from the black solid lines in figure 3, the fit results with the cutoff Λ =850 MeV are overall better than those with other cutoffs. For instance, the one with cutoff Λ =750 MeV describes better the imaginary part of the ${}^3S_1$ phase shift with $I = 1$ but the result for the real part is worse, whereas just the opposite is the case for the cutoff Λ =950 MeV. Thus, we adopt the potentials with cutoff Λ =850 MeV for the more detailed discussion below. The χ^2 is calculated for the S-matrix elements, in the same way as in ref. [61]: the uncertainty of the 'data' from the PWA are estimated following ref. [61], where we set $\Delta^2_{S_{LL'}} = 0.1$. It is found that the contribution from the $\bar{N}N$ 'data' to the total χ^2 is rather tiny. Indeed, the bulk of the obtained χ^2 stems from $e^+e^- \to \bar{N}N$ observables like integrated and differential cross sections, see the discussions in the following subsection.

JHEP08(2024)208

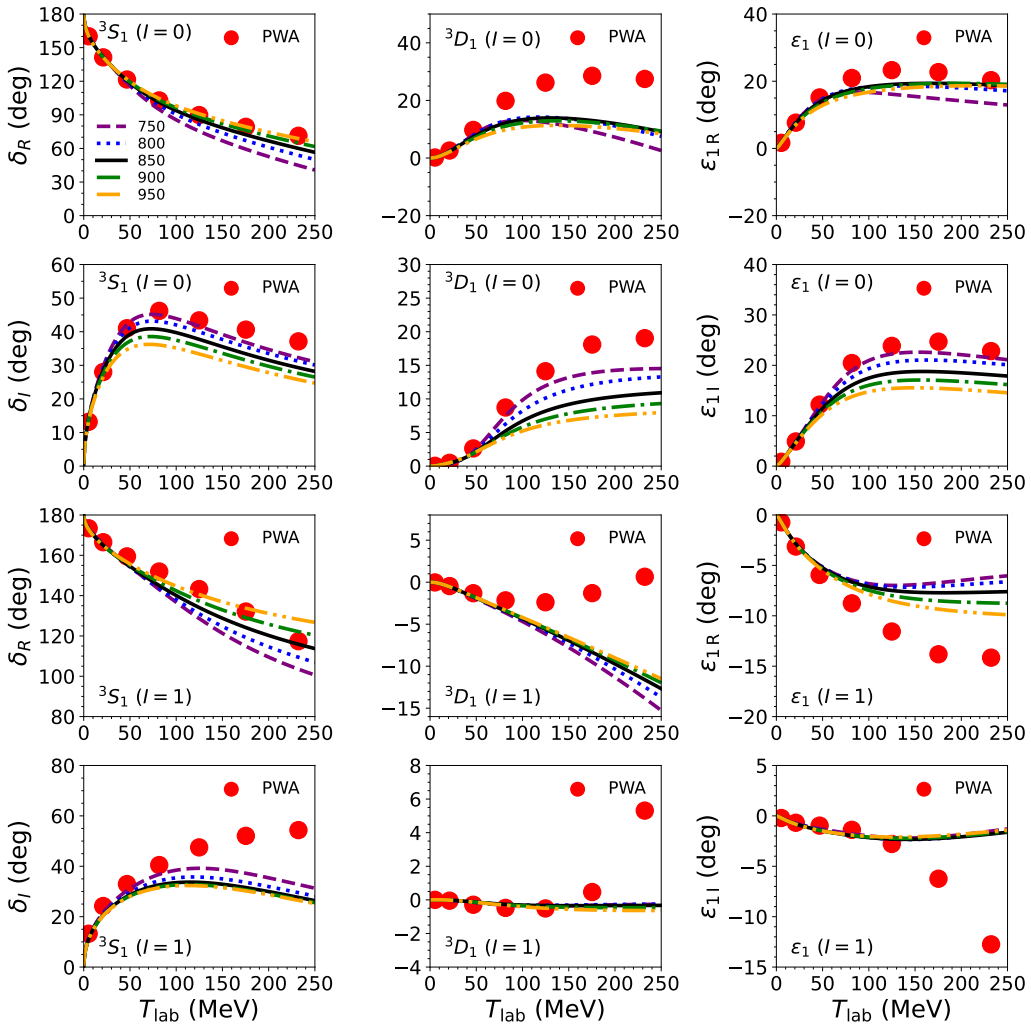

Figure 3. Real and imaginary parts of the phase shifts and inelasticities at NLO for the $^3S_1 - {}^3D_1$ partial waves, with isospin $I = 0$ and/or $I = 1$. The red-filled circles are the results of the PWA [62]. The green dashed, blue dotted, black solid, purple dash-dotted, and orange dash-dot-dotted lines represent our results with cutoffs Λ =750, 800, 850, 900, 950 MeV, respectively.

In figure 4, we provide our results for the phase shifts and inelasticities at LO and NLO for $\Lambda = 850$ MeV, shown as purple dashed and black solid lines, respectively. One can see that at LO the phase shifts and inelasticities of the PWA are well described in the very low-energy region, i.e. for $T_{\rm lab} \leq 25$ MeV, which includes the first two energy points of the PWA. In the NLO case, the 'data' are well reproduced up to $T_{\rm lab} \leq 50$ MeV, which concerns the first three points for each set. This is in line with the expected convergence pattern of χEFT. As mentioned above, the scattering lengths are included in the fitting procedure, too. The results are listed in table 2. The predictions by refs. [59, 61] are set to be the 'data'. The errors are set as $\Delta a = 0.1$ fm, considering the difference between the calculations at different chiral orders [59, 61]. Our scattering lengths are fairly close to those predicted by SU(2) χEFT.

The uncertainty is estimated following refs. [51, 61]. The main idea is to use the expected size of higher-order corrections for the estimation of the theoretical uncertainty.

JHEP08(2024)208

	LO	NLO				
Λ (MeV)	850	750	800	850	900	950
$\tilde{C}_{^{13}S_1}$ (GeV^{-2})	0.0098	1.3165	1.9390	2.8716	3.5020	4.5199
$C_{^{13}S_1}$ (GeV^{-4})	–	1.3422	1.0455	1.0649	0.9994	1.0601
$C_{^{1}\epsilon_1}$ (GeV^{-4})	–	2.4806	2.0745	1.9273	1.6603	1.3303
$\tilde{C}^a_{^{13}S_1}$ (GeV^{-1})	0.2730	-0.6431	-0.4821	-0.3219	0.0214	0.5517
$C^a_{^{13}S_1}$ (GeV^{-3})	–	-1.9000	-0.8156	-0.3697	-0.1217	0.0363
$C^a_{^{1}\epsilon_1}$ (GeV^{-3})	–	-2.0261	-1.4201	-1.0939	-0.8546	-0.6681
$C^a_{^{13}D_1}$ (GeV^{-3})	–	0.8432	0.0061	0.0000	0.0003	0.0000
$\tilde{C}_{^{33}S_1}$ (GeV^{-2})	-0.0531	-0.0356	-0.0289	-0.0235	-0.0304	-0.0509
$C_{^{33}S_1}$ (GeV^{-4})		0.1507	0.1620	0.1632	0.1727	0.1916
$C_{^{3}\epsilon_1}$ (GeV^{-4})		1.1900	0.9196	0.7727	0.6941	0.6482
$\tilde{C}^a_{^{33}S_1}$ (GeV^{-1})	-0.1614	0.0098	-0.0041	-0.0269	-0.0216	0.0215
$C^a_{^{33}S_1}$ (GeV^{-3})	–	0.4299	0.3937	0.4536	0.4970	0.5050
$C^a_{^{3}\epsilon_1}$ (GeV^{-3})	–	-4.7577	-3.4012	-2.5813	-2.1131	-1.8259
$C^a_{^{33}D_1}$ (GeV^{-3})	–	0.0001	0.0000	0.0000	0.0000	0.0000
$G_{\rm E}^{0(I=0)}$	0.2807	0.9222	1.0274	1.1795	1.2406	1.2669
$G_{\rm E}^{0(I=1)}$	-0.4174 +0.2979i	-0.0403 +0.5287i	-0.0057 +0.4872i	0.0385 +0.4494i	0.0746 +0.4134i	0.1048 +0.3781i
$N_p^{\rm BESIII\ 2019}$	6.0372	5.8976	5.9320	5.9734	5.9957	5.9902
$N_p^{\rm BESIII\ 2020}$	1.0277	0.9476	0.9495	0.9490	0.9468	0.9434
$N_p^{\rm BESIII\ 2021}$	18.2102	19.1115	19.1160	19.1184	19.1214	19.1258
$N_p^{\rm BaBar\ 2006}$	1.2101	1.1989	1.1987	1.1984	1.1983	1.1983
$N_p^{\rm BaBar\ 2013}$	1.2463	1.2189	1.2183	1.2173	1.2162	1.2149
$N_p^{\rm CMD-3\ 2016}$	1.3746	1.3274	1.3242	1.3225	1.3205	1.3169
$N_n^{\rm SND\ 2014}$	10.0870	9.9250	10.0633	10.2055	10.3328	10.4440
$N_n^{\rm SND\ 2019}$	0.6426	0.6740	0.6769	0.6678	0.6756	0.6685
$N_n^{\rm SND\ 2022}$	0.6065	0.5967	0.6043	0.6126	0.6210	0.6295

Table 1. Values of parameters at LO and NLO for different cutoffs. The superscript a indicates parameters that are related to the annihilation part in eqs. (A.37). Note that all the LECs are in units of 10^4 [61]. The normalization factors N are discussed in more detail later.

	This work: LO	This work: NLO	N^{2}LO [59]	N^{3}LO [61]
$a_{^3S_1}^{I=0}$(fm)	1.43–0.72i	1.35–0.94i	1.37–0.88i	1.42–0.88i
$a_{^3S_1}^{I=1}$(fm)	0.47–0.78i	0.45–0.79i	0.44–0.91i	0.44–0.96i

Table 2. Results of the $^3S_1$ scattering lengths (in fm) from SU(2) χEFT [59, 61] and from our fit.

JHEP08(2024)208

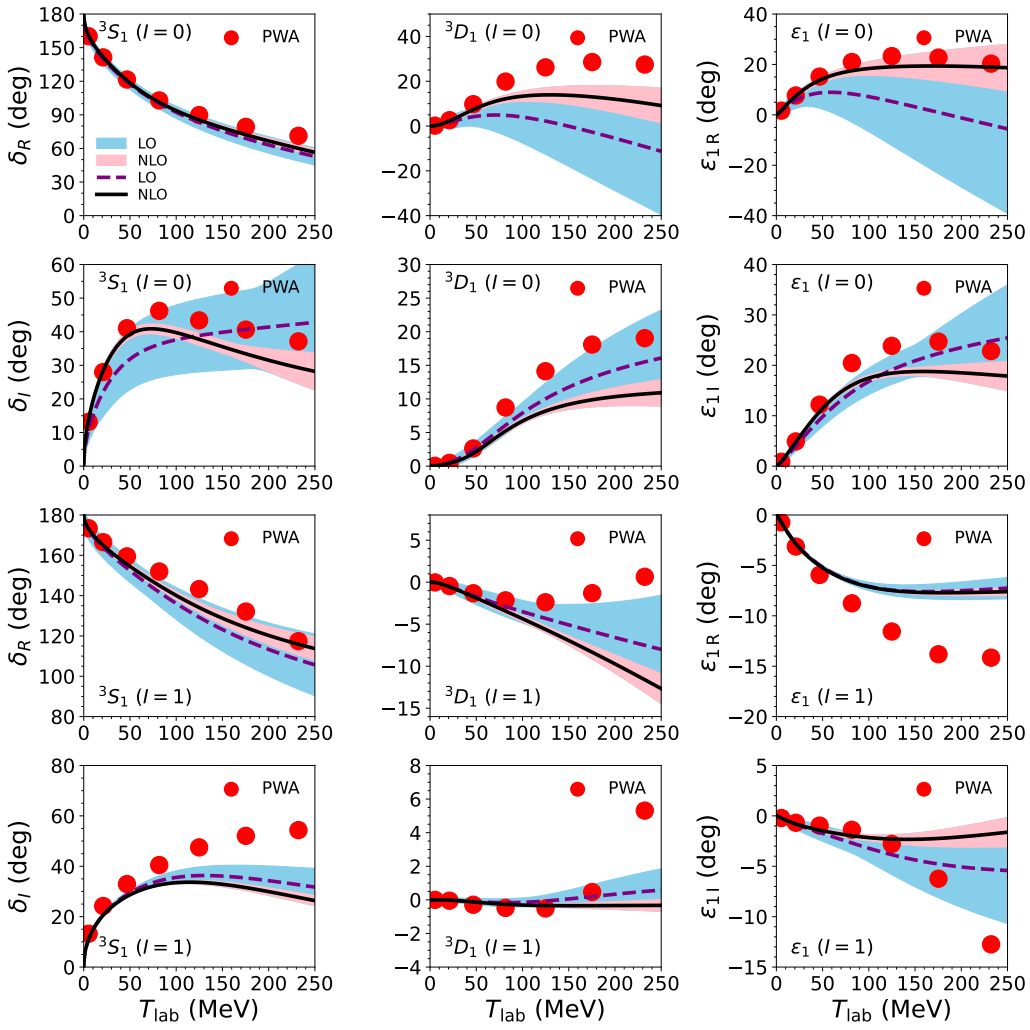

Figure 4. Real and imaginary parts of the phase shifts and inelasticities at LO and NLO in the $^3S_1 - {}^3D_1$ partial waves, with the isospin $I = 0, 1$. The red-filled circles are from the PWA [62]. The purple dashed and black solid lines are the results at LO and NLO with cutoff $\Lambda = 850\,\text{MeV}$, respectively, and the sky blue and pink bands are the corresponding uncertainties.

The uncertainty $\Delta X^{\rm NLO}(k)$ of the NLO prediction $X^{\rm NLO}(k)$ for a given observable $X(k)$ can be written as [51]

$$\Delta X^{\rm NLO}(k) = \max\left(Q^3 \times |X^{\rm LO}(k)|, Q \times |X^{\rm LO}(k) - X^{\rm NLO}(k)|\right), \tag{3.4}$$

with the parameter Q defined by

$$Q = \max\left(\frac{k}{\Lambda_b}, \frac{M_\pi}{\Lambda_b}\right), \tag{3.5}$$

where k is the c.m.f. momentum and Λ_b is the breakdown scale. Here we take Λ_b=900 MeV. Note that the quantity $X(k)$ represents either an observable such as a cross section or a derived quantity, e.g., phase shifts. This method is expected to provide a natural and more reliable estimate of the uncertainty than relying on cutoff variations.

JHEP08(2024)208

3.3 Fit to the e^+e^- observables

In this section, we discuss the results for the $e^+e^- \leftrightarrow \bar{N}N$ observables, i.e. cross sections, angular distributions, and EMFFs. For the relevant formulae, see eqs. (2.5)–(3.7). Note that these data and the ones for $\bar{N}N$ scattering are fitted simultaneously. For $e^+e^- \to \bar{p}p$, the data sets of cross sections are taken form ADONE [13], Fenice [17–19], DM1 [14], DM2 [15], BaBar [21, 22], CMD-3 [23, 24], BESIII [25, 27–29]. Data for $e^+e^- \to \bar{n}n$ are taken from Fenice [17, 19], SND [30, 31, 33] and BESIII [32, 34]. The $\bar{p}p \to e^+e^-$ cross sections are taken from PS170 [63]. However, it should be stressed that, since some old data sets have significant errors, we only include data published after 2005 in the actual fitting procedure, that is, the data from BaBar [21, 22], CMD-3 [23, 24], and BESIII [27–29] for $e^+e^- \to \bar{p}p$, and SND [30, 31, 33] and BESIII [32, 34] for $e^+e^- \to \bar{n}n$. An exception is made for the data by PS170 [63] since it is the only experimental information for the reaction $\bar{p}p \to e^+e^-$.

Our fits to the cross sections for $e^+e^- \to \bar{p}p$, $\bar{n}n$, and $\bar{p}p \to e^+e^-$ are summarized in figure 5. The four graphs at the top are the fit results for LO (purple dashed) and NLO (black solid) for the cutoff $\Lambda = 850\,\text{MeV}$, with the corresponding error bands in the colors sky-blue and pink, respectively. The four graphs at the bottom are NLO results with different cutoffs: the purple dashed, blue dotted, black solid, green dash-dotted, and orange dash-dot-dotted lines are for cutoffs 750, 800, 850, 900, and 950 MeV, respectively. As can be seen, the LO results are consistent with the data up to roughly 2 GeV, while the NLO results agree with the experiments rather well over the whole considered energy region, for all cutoffs.

Obviously, the $e^+e^- \to \bar{N}N$ cross sections rise very quickly from the $\bar{N}N$ thresholds, see figure 5. Then, for $e^+e^- \to \bar{p}p$, the cross section remains unchanged up to roughly 2 GeV, and eventually starts to decrease. Regarding $\bar{p}p \to e^+e^-$, the inverse process of the former, the cross-section decreases rapidly with energy. The difference in the behavior can be easily understood from the relation between the reaction cross sections, $\sigma_{\bar{p}p\to e^+e^-} \simeq (k_e^2/k_N^2)\,\sigma_{e^+e^-\to\bar{p}p}$ which follows from time reversal invariance [40]. For the cross section of the process $e^+e^- \to \bar{n}n$, see the left side graphs in the second and fourth rows of figure 5, there is also a strong rise near the threshold, but the situation for the proton and neutron cases is a bit different: the one for the neutron starts to decrease rapidly at 1.9 GeV. As discussed in ref. [10], this reveals that the oscillation of the so-called subtracted form factors (SFFs) of the neutron and proton are different. The ratio of the cross sections,

$$R_{np} = \sigma(e^+e^- \to \bar{n}n)/\sigma(e^+e^- \to \bar{p}p)\,, \tag{3.6}$$

are essential to refine the analysis. As can be found, ours fit the data well. See the last graph in the second and fourth rows. Nevertheless, in the low-energy region, the statistics of the data is poor. It would be rather helpful to perform more experiments in the energy region closer to the $\bar{N}N$ thresholds.

Experimental results for the angular distributions of $e^+e^- \to \bar{p}p$ are available for the energy intervals of 1.877–1.950 GeV/c^2, 1.950–2.025 GeV/c^2, 2.025–2.100 GeV/c^2, 2.100–2.200 GeV/c^2, 1.920–2.000 GeV/c^2, 2.000–2.300 GeV/c^2, 1.920–2.000 GeV/c^2, and at 2.000, 2.050, 2.100, 2.125, 2.150, 2.175, 2.2 GeV/c^2. The data are taken from the works of the BESIII [27–29], BaBar [21, 22], and CMD-3 [24] collaborations. In ref. [63], angular distributions for $\bar{p}p \to e^+e^-$ can be found at the energies $\sqrt{s}$=1.9200, 1.9391, 1.9574, 1.9840,

JHEP08(2024)208

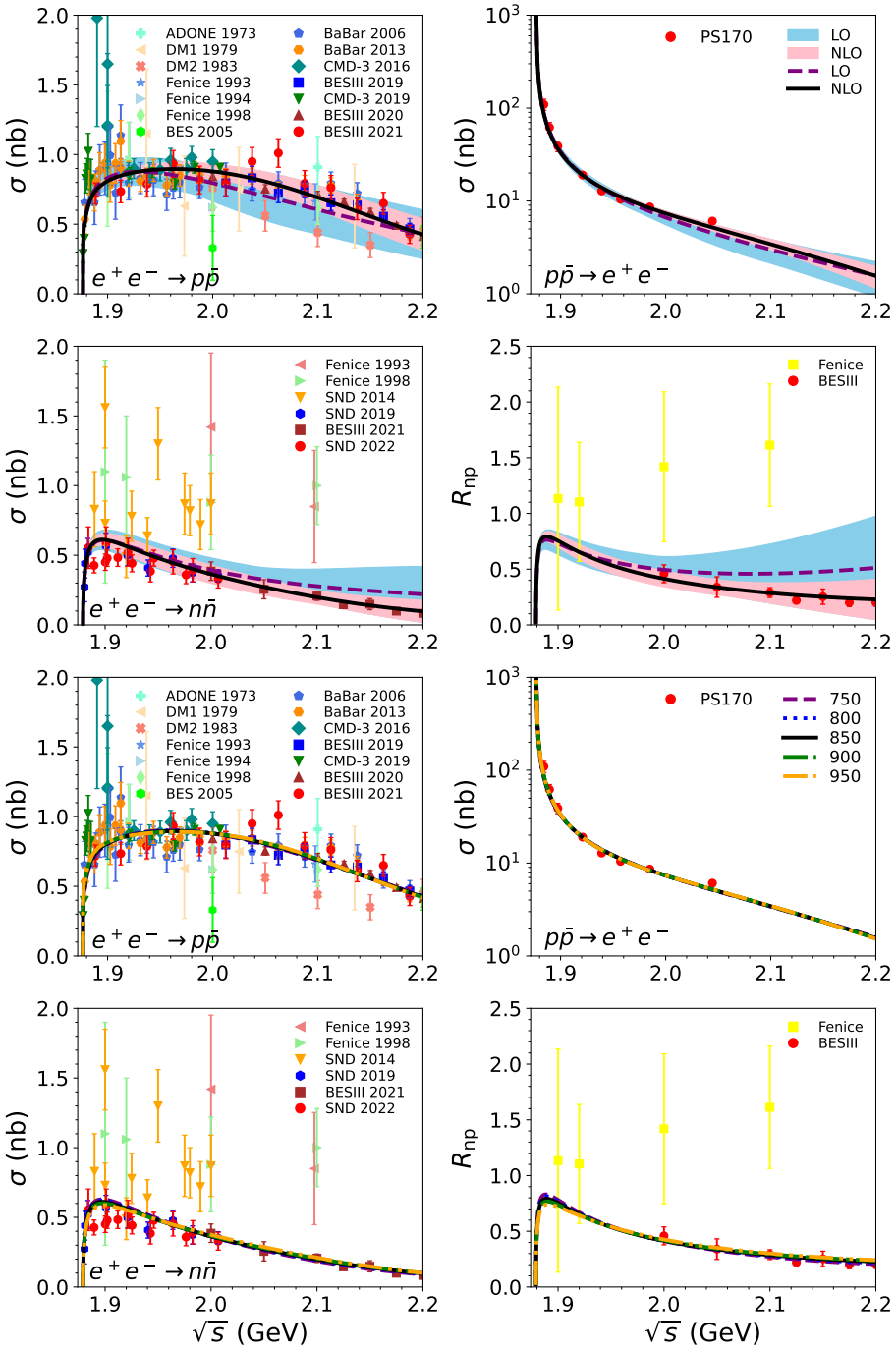

Figure 5. The comparison between our fit results and the experimental data sets of cross sections, including the processes of $e^+e^- \to \bar{p}p$, $\bar{n}n$, and $\bar{p}p \to e^+e^-$. The experimental data sets are taken from ADONE [13], Fenice [17–19], DM1 [14], DM2 [15], BaBar [21, 22], CMD-3 [23, 24], BESIII [25, 27–29], SND [30, 31, 33], and PS170 [63].

JHEP08(2024)208

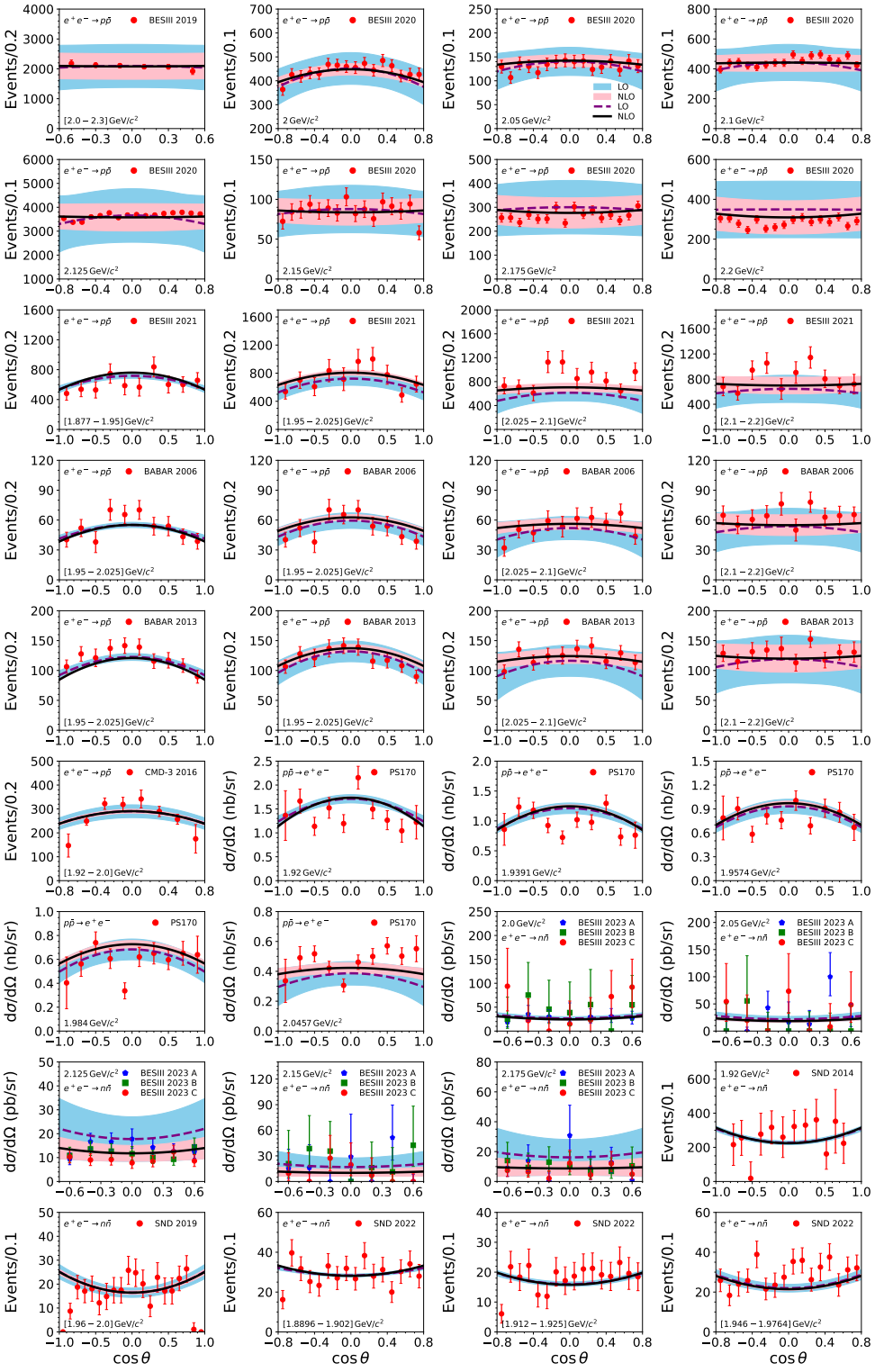

Figure 6. Our fit to the angular distributions of the processes of $e^+e^- \to \bar{p}p$, $\bar{n}n$, and $\bar{p}p \to e^+e^-$. The experimental data are taken from BESIII [27–29, 34], BaBar [21, 22], CMD-3 [24], SND [30, 31, 33] and PS170 [63].

JHEP08(2024)208

	LO		NLO					
	N	χ^2/N	N	χ^2/N				
Λ (MeV)		850		750	800	850	900	950
Cross Section	105	1.59	154	1.70	1.65	1.58	1.53	1.48
Differential cross section	221	1.31	477	1.59	1.57	1.53	1.49	1.47
R_{np}	1	0.20	7	0.38	0.62	0.99	1.41	1.76
$\lvert G_{\rm E}/G_{\rm M}\rvert$, $\lvert G_{\rm E}\rvert$ and $\lvert G_{\rm M}\rvert$	13	0.54	44	1.74	1.70	1.60	1.42	1.22
Phase shift	24	0.008	36	0.003	0.004	0.004	0.005	0.006
Scattering length	4	1.41	4	0.86	0.92	0.93	0.87	0.84
total	368	1.28	722	1.53	1.50	1.46	1.42	1.38

Table 3. The χ^2/N of cross section, differential cross section, $|G_{\rm E}/G_{\rm M}|$, $|G_{\rm E}|$, $|G_{\rm M}|$ and R_{np} for the LO and NLO fits. In the last row we list the total χ^2/N to provide an overview of the fit quality.

and 2.0457 GeV. Angular distributions for $e^+e^- \to \bar{n}n$ were measured at energy intervals of 1.960–2.000, 1.8896–1.9020, 1.9120–1.9250, and 1.9460–1.9764 GeV/c^2, and at the energies $\sqrt{s}$=1.920, 2.000, 2.050, 2.125, 2.150, end 2.175 GeV/c^2. They are taken from the SND [30, 31, 33] and BESIII [34] experiments.

A visual comparison between our results and the data is provided in figure 6. The purple dashed and black solid lines are the results at LO and NLO, respectively. Correspondingly, the sky-blue and pink bands are the uncertainties of LO and NLO, calculated from eq. (3.4). Notice that for each data set of the event distribution we apply one constant normalization factor for all energy values. For instance, for all the data points of BESIII in the year 2020 [28], as shown in the first two rows, the normalization factor is labeled as $N_p^{\rm BESIII\,2020}$.

As can be seen from figure 6, our fit is of high quality, and this confirms the reliability of our analysis. The graphs of the first six rows and the first two graphs in the seventh row are our results for the angular distributions for $e^+e^- \to \bar{p}p$ and $\bar{p}p \to e^+e^-$, where the last five graphs in the indicated places are that for the latter reaction. The results for $e^+e^- \to \bar{p}p$ are better than that of the $\bar{p}p \to e^+e^-$. This is partly caused by the lower statistics of the latter data. Nevertheless, the $\bar{p}p \to e^+e^-$ differential cross-section data have no normalization factors, and ours are consistent with them within the errors. The graphs in the three bottom rows (except for the first two graphs) are our fits to the data sets of the angular distributions of $e^+e^- \to \bar{n}n$. The data for the differential cross section have significant uncertainties except for the one at the energy point $\sqrt{s} = 2.125$ GeV. Our results agree well with these data points, too. The data on the angular distributions have more minor errors, but the fit quality is not as good as for the other two processes, $e^+e^- \to \bar{p}p$ and $\bar{p}p \to e^+e^-$. Nevertheless, our results are still compatible with the data sets except for a few points near $\cos\theta = \pm 1$. Notice that the measurements are difficult to perform close to $\cos\theta = \pm 1$. In order to provide a quantitative overview of the quality of our results, we summarize the χ^2 values of the fits for each cutoff Λ in table 3. As can be seen, most of the available data are for total and differential cross sections. For each kind of data set, our fits yield a χ^2/N around one, where N is the number of data points, while the contributions from phase shifts (by fitting to the S-matrix elements) and scattering lengths are tiny. Finally, the total χ^2/N can be found in the last row of table 3.

JHEP08(2024)208

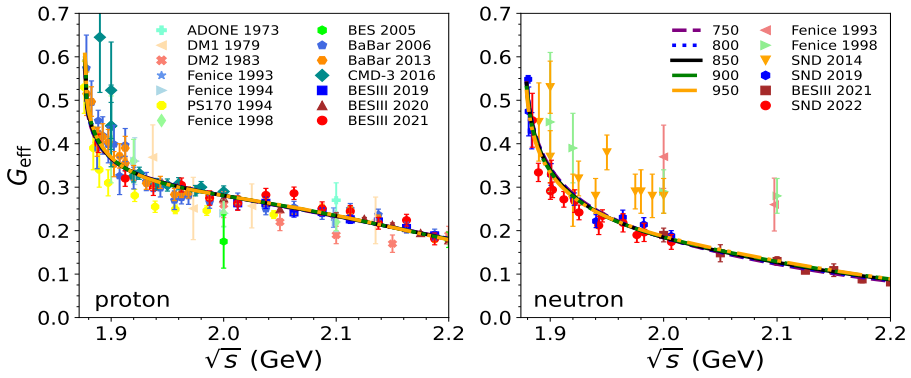

Figure 7. The comparison between our results and the experimental datasets of effective EMFFs. The experimental data sets are taken from ADONE [13], Fenice [17–19], DM1 [14], DM2 [15], BaBar [21, 22], CMD-3 [23], BESIII [25, 27–29, 32], SND [30, 31, 33], PS170 [63].

The value for the fit with cutoff $\Lambda = 850\,\text{MeV}$ is about 1.46. This indicates that our fit is of high quality and it can be used to extract the individual EMFFs reliably.

3.4 Effective EMFFs and oscillations

The effective EMFF, $|G_{\rm eff}|$, is basically a parameterization of the total cross section, cf. eq. (3.8), which is provided by many experimental groups. Ignoring the electron mass, the cross section is given by

$$\sigma = \frac{4\pi\alpha^2\beta}{3s} C(s) \left[|G_{\rm M}^N(s)|^2 + \frac{2M_N^2}{s} |G_{\rm E}^N(s)|^2 \right] . \tag{3.7}$$

By defining $G_{\rm E}^N = G_{\rm M}^N \equiv G_{\rm eff}^N$ the modulus of the effective EMFFs can be evaluated directly from the integrated cross section [13, 14],

$$|G_{\rm eff}(s)| = \sqrt{\frac{\sigma_{e^+e^-\to\bar{N}N}(s)}{\frac{4\pi\alpha^2\beta}{3s} C(s) \left[1 + \frac{2M_N^2}{s}\right]}}. \tag{3.8}$$

Our results are presented in figure 7. The graph on the left side shows the effective EMFF of the proton, and the one on the right side is that of the neutron. The purple dashed, blue dotted, black solid, green dash-dotted, and orange dash-dot-dotted lines are our results at NLO with cutoffs Λ =750, 800, 850, 900, 950 MeV, respectively. Obviously, these lines overlap with each other, and for all cutoffs an excellent description of the effective EMFFs is obtained. The effective EMFFs of the proton and the neutron exhibit similarities and differences. Both effective EMFFs fall off rapidly at energies near the $\bar{N}N$ threshold, and then much more slowly with increasing energy. However, there is a difference in the magnitude, with the effective form factor of the proton being noticeably larger than that of the neutron.

As mentioned in the Introduction, an interesting phenomenon was discovered in the analysis of the experiment concerning these effective EMFFs: they show an oscillatory behavior, a feature which is prominently exposed once a dipole contribution is subtracted [3].

JHEP08(2024)208

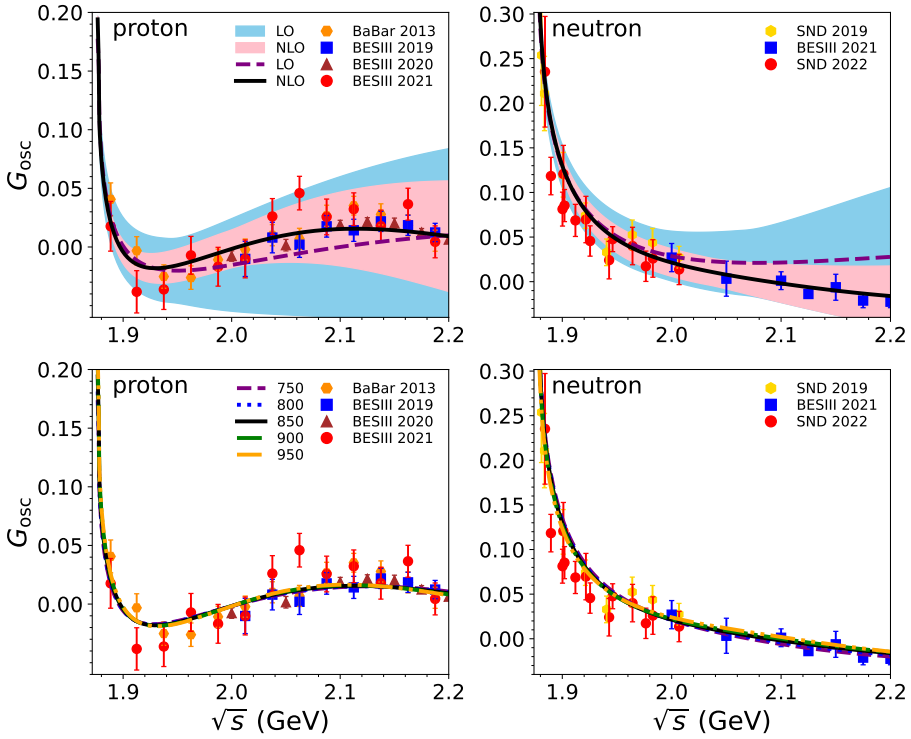

Figure 8. Comparison between the SFFs deduced from the experiments and our predictions. The purple dashed and black solid lines are our results at LO and NLO, with the corresponding error bands in sky blue and pink, respectively. The cutoff is chosen to be $\Lambda = 850\,\text{MeV}$. The experimental information is from BaBar [21, 22], BESIII [28, 29], and SND [31, 33].

Moreover, ref. [32] revealed that there is a phase difference between the oscillation of the subtracted form factors (SFFs) of the proton and neutron. These SFFs are defined as the difference between the effective EMFFs and the dipole contribution [3, 29, 32],

$$G_{\text{osc}}(s) = |G_{\text{eff}}| - G_D(s)\,, \tag{3.9}$$

where G_D is the dipole function given in [3, 29]

$$G_D^p(s) = \frac{\mathcal{A}_p}{(1+s/m_a^2)[1-s/q_0^2]^2}\,,$$
$$G_D^n(s) = \frac{\mathcal{A}_n}{[1-s/q_0^2]^2}\,,$$

with parameters fixed to $\mathcal{A}_p$=7.7, $\mathcal{A}_n$=3.5±0.1, m_a^2=14.8 $(\text{GeV}/c)^2$ and q_0^2=0.71 $(\text{GeV}/c)^2$. For describing the SFF, in ref. [3] a function was suggested which consists of a damping factor and a periodic piece, namely $G_{osc} \equiv A\exp(-Bp)\cos(Cp+D)$. Here p is the momentum of the antinucleon in the rest-frame of the nucleon while the parameters A, B, C, D fix the overall normalization, the damping, the oscillation period and the so-called phase, respectively. When applying these formulae to the latest measurements of $e^+e^- \to \bar{p}p$ [29] and $e^+e^- \to \bar{n}n$ [32] by the BESIII Collaboration, a phase difference in the oscillations of the EMFFs of $\Delta = |D_p - D_n| = (125 \pm 12)^\circ$ was established.

JHEP08(2024)208

Let us briefly discuss the oscillations of the SFFs in the energy region below 2.2 GeV. The results are similar to the ones in our earlier paper [10]. Our predictions for the SFFs are shown in figure 8. They are evaluated via eq. (3.9), by using directly $G_{\rm eff}$, obtained by eq. (3.8) from the calculated $e^+e^- \to \bar{N}N$ cross sections. We recall that in the present analysis, the $\bar{N}N$ FSI is taken into account, and our results are compatible with most of the available data around the thresholds. This is different in some other pertinent studies in the literature.

As can be seen already from figure 7, in the energy region up to $\sqrt{s} = 2.2$ MeV no obvious oscillation pattern of effective EMFF is visible, neither for the proton nor for the neutron. After subtracting the contribution of the dipole, there is a distinct energy dependence in the SFFs, more pronounced for the proton than for the neutron, cf. figure 8. This energy dependence can be reproduced by our calculation which includes the $\bar{N}N$ FSI, but not by some simple functions like A/s^2. Besides, it looks like that there is no phase difference between the SFFs ($G_{\rm osc}$) of the proton and that of the neutron. Actually, in both cases the value at the respective thresholds is almost the same. In fact, in our earlier paper [10], the SFFs of the nucleons can be described by two fractional oscillators: one is the overdamped oscillator that dominates in the low-energy region, and the other is the underdamped oscillator that dominates in the high-energy region above 2 GeV. It is worth pointing out that there is a phase difference between the underdamped oscillators of the proton and the neutron, but there is no such difference in the overdamped ones. Our present results of the invisible oscillation in the low-energy region is consistent with the overdamped oscillators of our earlier paper [10]. Of course, this conclusion remains to be checked by more accurate measurements near the threshold in future experiments.

3.5 Individual EMFFs

From the reaction amplitude one can also extract the individual EMFFs. Results of $G_{\rm E}$ and $G_{\rm M}$, and their ratio $G_{\rm E}/G_{\rm M}$, including both the moduli and the phases, are shown in figure 9. The graphs in the first two columns are our results at LO and NLO, with cutoff $\Lambda = 850$ MeV, where the purple dashed and black solid lines are for LO and NLO, with the corresponding error bands sky blue and pink, respectively. The graphs in the last two columns are the results at NLO with different cutoffs, $\Lambda = 750, 800, 850, 900, 950$ MeV, corresponding to the purple dashed, blue dotted, black solid, green dash-dotted, and orange dash-dot-dotted lines, respectively. There are only a few published points for the modulus of the individual EMFFs, and our results are consistent with them.

The electric and magnetic form factors exhibit a similar behavior as the effective EMFFs, i.e. all of them decrease rapidly around the thresholds and more slowly for higher energies. Regarding the proton, the electric form factor decreases more rapidly with increasing $\sqrt{s}$ above 2 GeV, compared with the magnetic form factor. In case of the neutron it is the opposite. The ratio $|G_{\rm E}/G_{\rm M}|$ is shown in the graphs of the third row of figure 9. Both of the ratios start from unity at the threshold by definition. However, the one of the proton increases above $|G_{\rm E}/G_{\rm M}| = 1$ immediately after the threshold and then decreases with increasing energy $\sqrt{s}$, while the ratio of the neutron form factors decreases around the threshold and then increases as the energy increases. For the proton, the turning point of the ratio is at around 1.9 GeV, while that of the neutron is at 2.0 GeV. Interestingly, it looks as if both of them will go back to unity at higher energies, implying that $|G_{\rm E}|$ would become equal to $|G_{\rm M}|$ again in the high-energy region. This can be checked by future experiments.

JHEP08(2024)208

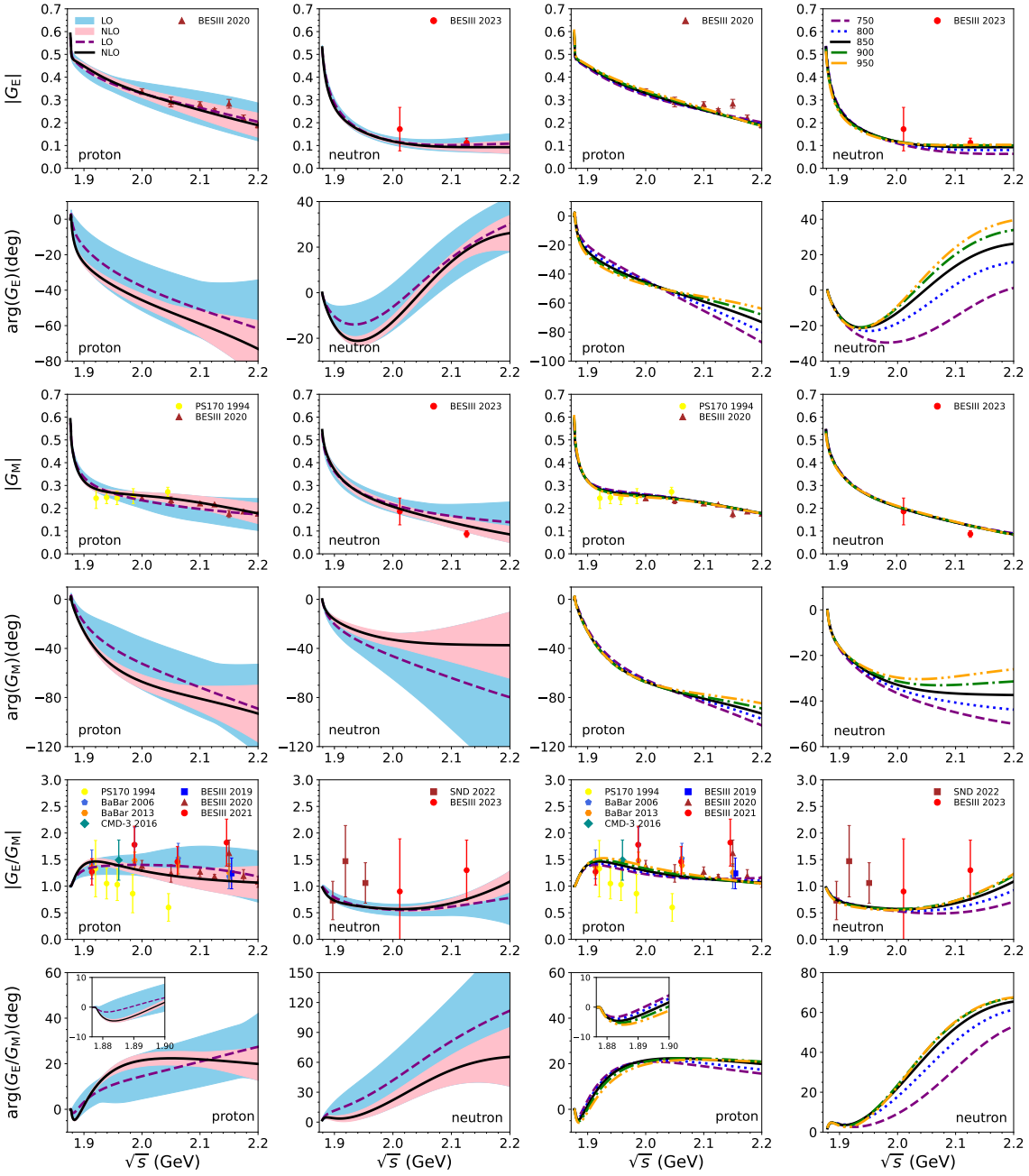

Figure 9. Predictions for the individual EMFFs, $G_{\rm E}$, $G_{\rm M}$, and the ratios $G_{\rm E}/G_{\rm M}$, including the modulus and the phases. The data shown in the graphs are taken from BaBar [21, 22], CMD-3 [23], BESIII [27–29, 34], SND [33], PS170 [63]. The results in the left two columns are for the cutoff $\Lambda = 850\,\text{MeV}$.

JHEP08(2024)208

At the threshold our results for $|G_M|$ and $|G_E|$ are slightly larger than those obtained by phenomenological fits, see, e.g., refs. [4, 34]. This is a consequence of the fact that in our calculation the effects of the $\bar{N}N$ interaction are taken into account explicitly. It leads to an enhancement of the cross section and, accordingly, of the EMFFs at low energies which cannot be described by simple parameterizations of the form factors [3, 34].

The phases of the EMFFs are shown in the second, fourth, and sixth rows of figure 9. Note that there can be an overall phase factor for the individual EMFFs, which can not be observed. Therefore, we set all the phases to be zero at the relevant thresholds. The variations of the phases with the energies are much more pronounced than those of the modulus. As can be seen, the phases of all the individual EMFFs decrease monotonously as the energy increases, except for that of the electric form factors of the neutron, which decreases first and then increases. It may indicate the difference between the charge of the valence quarks for the proton and the neutron. Interestingly, there is a peculiar behavior of the phases of $G_{\rm E}/G_{\rm M}$ very close to the thresholds, see the insets in the last row of figure 9 (and also figure 8 in [40]). Obviously the phase between the electric and the magnetic form factors varies significantly in the low-energy region, i.e. over the first 100 MeV or so. This is not caused by the mass difference between the proton and neutron which is ignored since the $\bar{N}N$ scattering amplitudes are evaluated in the isospin basis. Actually, the turning point of the phase is at roughly 1.883 GeV, i.e. above the thresholds of $\bar{p}p$ or $\bar{n}n$. We note that the electric and magnetic form factors have almost no phase difference without FSI. Also, the phase difference is much smaller for the LO results, where the D-wave contributions are smaller.[3] The strong variation for the NLO FSI reveals that there is a remarkable sensitivity, reflected in the properties of the EMFFs near the threshold. This is interesting and deserves further study through both theory and experiment.

4 Conclusions

In this paper we evaluated the individual EMFFs of the proton and neutron in the processes $e^+e^- \to \bar{p}p$ and $e^+e^- \to \bar{n}n$. The final-state interaction between antinucleon and nucleon is taken into account. The latter is based on an $\bar{N}N$ scattering amplitude generated from an $\bar{N}N$ potential derived within SU(3) χEFT up to NLO. It is included in the calculation of the integrated and differential cross sections of the processes $e^+e^- \to \bar{N}N$ within the DWBA.

An excellent description of the available data on the reaction $e^+e^- \to \bar{N}N$ up to 2.2 GeV is achieved. Specifically, our calculations also reproduce the strong enhancement of the cross sections near the $\bar{N}N$ thresholds observed in both processes. The individual EMFFs, $G_{\rm E}$ and $G_{\rm M}$, of the proton and neutron, and their ratio $G_{\rm E}/G_{\rm M}$, including the modulus and the phases, are predicted. It turned out that the phases of the electric form factors of the proton and the neutron are quite different. Interestingly, it is found that the relation $|G_{\rm E}| = |G_{\rm M}|$, strictly valid at the $\bar{N}N$ threshold, is eventually restored in the higher-energy region.

More accurate measurements near the threshold, hopefully performed in the near future, will be essential to get more precise constraints on electric and magnetic form factors of the nucleons and are important to refine our analysis. This will be helpful to understand the properties of the nucleons as well as the strong interaction.

[3] In ref. [64] a similar behavior is observed in the LO calculation of the EMFFs of Λ_c. However, the one in ref. [64] is more flat. This is so because in the $\Lambda_c^+\bar{\Lambda}_c^-$ case there is no D-wave contribution at LO.

JHEP08(2024)208

Acknowledgments

This work is supported by the National Natural Science Foundation of China (NSFC) with Grants No.12322502, 12335002, 11805059, 11675051, Joint Large Scale Scientific Facility Funds of the NSFC and Chinese Academy of Sciences (CAS) under Contract No.U1932110, Hunan Provincial Natural Science Foundation with Grant No. 2024JJ3004, and Fundamental Research Funds for the central universities. It was further supported by Deutsche Forschungsgemeinschaft (DFG) and NSFC through funds provided to the Sino-German CRC 110 "Symmetries and the Emergence of Structure in QCD" (NSFC Grant No. 11621131001, DFG Project-ID 196253076-TRR 110). The work of UGM was supported in part by the CAS President's International Fellowship Initiative (PIFI) (Grant No. 2025PD0022).

A The potential for the $\bar{N}N$ interaction

A.1 Lagrangians of SU(3) χEFT

The calculation of nucleon-nucleon and nucleon-hyperon scatterings within SU(3) χEFT has been given in ref. [54]. Here, we focus on the direct calculation of antinucleon-nucleon scattering based on SU(3) χEFT, too. Note that most of the formulas in the present paper are similar to those in ref. [54]. However, for the convenience of the readers, we list all the details here. The interaction Lagrangian of baryons coupling to mesons can be obtained from SU(3) χEFT [54, 65],

$$\mathcal{L}_{MB} = \langle \bar{B}(i\gamma^\mu D_\mu - M_0)B\rangle - \frac{D}{2}\langle \bar{B}\gamma^\mu\gamma^5\{u_\mu, B\}\rangle - \frac{F}{2}\langle \bar{B}\gamma^\mu\gamma^5[u_\mu, B]\rangle\,, \tag{A.1}$$

where $\langle\cdots\rangle$ denotes the flavor trace, and the covariant derivative is $D_\mu B = \partial_\mu B + [\Gamma_\mu, B]$, with $\Gamma_\mu = \frac{1}{2}(u^\dagger\partial_\mu u + u\partial_\mu u^\dagger)$. Here, one has $u_\mu = i(u^\dagger\partial_\mu u - u\partial_\mu u^\dagger)$ and $u = \exp(i\Phi/\sqrt{2}f_0)$, where f_0 is the Goldstone boson decay constant in the three-flavor chiral limit, and M_0 is the baryon mass in the three-flavor chiral limit. F and D are coupling constants which satisfy $F + D = g_A \simeq 1.27$. The baryon octet matrix B and the meson octet matrix Φ have the following forms

$$\Phi = \begin{pmatrix} \frac{\pi^0}{\sqrt{2}} + \frac{\eta}{\sqrt{6}} & \pi^+ & K^+ \\ \pi^- & -\frac{\pi^0}{\sqrt{2}} + \frac{\eta}{\sqrt{6}} & K^0 \\ K^- & \bar{K}^0 & -\frac{2\eta}{\sqrt{6}} \end{pmatrix}, \quad B = \begin{pmatrix} \frac{\Sigma^0}{\sqrt{2}} + \frac{\Lambda}{\sqrt{6}} & \Sigma^+ & p \\ \Sigma^- & -\frac{\Sigma^0}{\sqrt{2}} + \frac{\Lambda}{\sqrt{6}} & n \\ -\Xi^- & \Xi^0 & -\frac{2\Lambda}{\sqrt{6}} \end{pmatrix}. \tag{A.2}$$

After expanding the Lagrangian in eq. (A.1), the relevant interaction Lagrangians of the one- and two-mesons coupling with baryons can be obtained as

$$\begin{aligned} \mathcal{L}_{BB\Phi} &= -\frac{\sqrt{2}}{2f_0}(D\langle \bar{B}\gamma^\mu\gamma^5\{\partial_\mu\Phi, B\}\rangle + F\langle \bar{B}\gamma^\mu\gamma^5[\partial_\mu\Phi, B]\rangle)\,, \\ \mathcal{L}_{BB\Phi\Phi} &= \frac{i}{4f_0^2}\langle \bar{B}\,[[\Phi, \partial_\mu\Phi], B]\rangle\,. \end{aligned} \tag{A.3}$$

The concrete form of the interaction Lagrangians can be obtained by taking the flavor trace,

$$\begin{aligned}
\mathcal{L}_{BB\Phi} = & -f_{NN\pi}\left(\bar{p}\gamma^\mu\gamma^5 p\partial_\mu\pi^0 - \bar{n}\gamma^\mu\gamma^5 n\partial_\mu\pi^0 + \sqrt{2}\bar{p}\gamma^\mu\gamma^5 n\partial_\mu\pi^+ + \sqrt{2}\bar{n}\gamma^\mu\gamma^5 p\partial_\mu\pi^-\right) \\
& - f_{\Lambda NK}\left(\bar{\Lambda}\gamma^\mu\gamma^5 p\partial_\mu K^- + \bar{p}\gamma^\mu\gamma^5\Lambda\partial_\mu K^+ + \bar{\Lambda}\gamma^\mu\gamma^5 n\partial_\mu\bar{K}^0 + \bar{n}\gamma^\mu\gamma^5\Lambda\partial_\mu K^0\right) \\
& - f_{\Sigma NK}\Big(\bar{\Sigma}^0\gamma^\mu\gamma^5 p\partial_\mu K^- + \bar{p}\gamma^\mu\gamma^5\Sigma^0\partial_\mu K^+ + \sqrt{2}\bar{\Sigma}^-\gamma^\mu\gamma^5 p\partial_\mu\bar{K}^0 + \sqrt{2}\bar{p}\gamma^\mu\gamma^5\Sigma^+\partial_\mu K^0 \\
& + \sqrt{2}\bar{\Sigma}^+\gamma^\mu\gamma^5 n\partial_\mu K^- + \sqrt{2}\bar{n}\gamma^\mu\gamma^5\Sigma^-\partial_\mu K^+ - \bar{\Sigma}^0\gamma^\mu\gamma^5 n\partial_\mu\bar{K}^0 - \bar{n}\gamma^\mu\gamma^5\Sigma^0\partial_\mu K^0\Big) \\
& - f_{NN\eta}\left(\bar{p}\gamma^\mu\gamma^5 p\partial_\mu\eta + \bar{n}\gamma^\mu\gamma^5 n\partial_\mu\eta\right) + \cdots, \\
\mathcal{L}_{BB\Phi\Phi} = & \frac{i}{4f_0^2}\Big[\bar{p}\gamma^\mu p(\pi^+\partial_\mu\pi^- - \pi^-\partial_\mu\pi^+) - \bar{n}\gamma^\mu n(\pi^+\partial_\mu\pi^- - \pi^-\partial_\mu\pi^+) \\
& - \sqrt{2}\bar{p}\gamma^\mu n(\pi^+\partial_\mu\pi^0 - \pi^0\partial_\mu\pi^+) - \bar{n}\gamma^\mu p(\pi^0\partial_\mu\pi^- - \pi^-\partial_\mu\pi^0) \\
& + 2\bar{p}\gamma^\mu p(K^+\partial_\mu K^- - K^-\partial_\mu K^+) + \bar{n}\gamma^\mu n(K^+\partial_\mu K^- - K^-\partial_\mu K^+) \\
& + \bar{p}\gamma^\mu p(K^0\partial_\mu\bar{K}^0 - \bar{K}^0\partial_\mu K^0) + 2\bar{n}\gamma^\mu n(K^0\partial_\mu\bar{K}^0 - \bar{K}^0\partial_\mu K^0) \\
& + \bar{p}\gamma^\mu n(K^+\partial_\mu\bar{K}^0 - \bar{K}^0\partial_\mu K^+) + \bar{n}\gamma^\mu p(K^0\partial_\mu K^- - K^-\partial_\mu K^0)\Big] + \cdots,
\end{aligned} \tag{A.4}$$

where '$\cdots$' represents terms that will not be used in the calculation of the $\bar{N}N$ scattering potentials up to NLO. The coupling constants are given as [54],

$$\begin{aligned}
& f_{NN\pi} = f, \quad f_{NN\eta} = \frac{1}{\sqrt{3}}(4\alpha - 1)f, \\
& f_{\Lambda NK} = -\frac{1}{\sqrt{3}}(1 + 2\alpha)f, \quad f_{\Sigma NK} = (1 - 2\alpha)f\,,
\end{aligned} \tag{A.5}$$

with $\alpha = F/(F + D)$ and $f = g_A/2f_0$. The calculation will be performed in the framework of old-fashioned time-ordered perturbation theory [66]. The interaction Hamiltonians are needed and are defined as

$$W_I = -\int \mathrm{d}\boldsymbol{x}^3[\mathcal{L}_I(x)]_{x^0=0}\,, \tag{A.6}$$

where $\mathcal{L}_I$ is the Lagrangians of $\mathcal{L}_{BB\Phi}$ and $\mathcal{L}_{BB\Phi\Phi}$ as given in eq. (A.4).

A.2 The OBE potential

In practice, the $\bar{N}N$ scattering equation is solved in the isospin basis. Hence, we first calculate the potentials in the physical basis according to time-ordered perturbation theory and then transform them into the isospin basis. In the physical basis, one has $V_{\bar{p}p\to\bar{p}p} = V_{\bar{n}n\to\bar{n}n}$ and $V_{\bar{p}p\to\bar{n}n} = V_{\bar{n}n\to\bar{p}p}$, neglecting isospin breaking. The relation of the potentials between the physical and isospin bases satisfies

$$V_{\bar{p}p\to\bar{p}p} = \frac{1}{2}(V_{\bar{N}N}^{I=0} + V_{\bar{N}N}^{I=1}), \quad V_{\bar{p}p\to\bar{n}n} = \frac{1}{2}(V_{\bar{N}N}^{I=0} - V_{\bar{N}N}^{I=1})\,. \tag{A.7}$$

As a result, only $V_{\bar{p}p\to\bar{p}p}$ and $V_{\bar{p}p\to\bar{n}n}$ are needed to determine the whole potential. The contributions to the $\bar{N}N$ potential up to NLO are shown in figure 10, and consist of OBEs, TBEs, and contact terms. The TBE potentials include football, left and right triangle, planar, and cross box diagrams.

JHEP08(2024)208

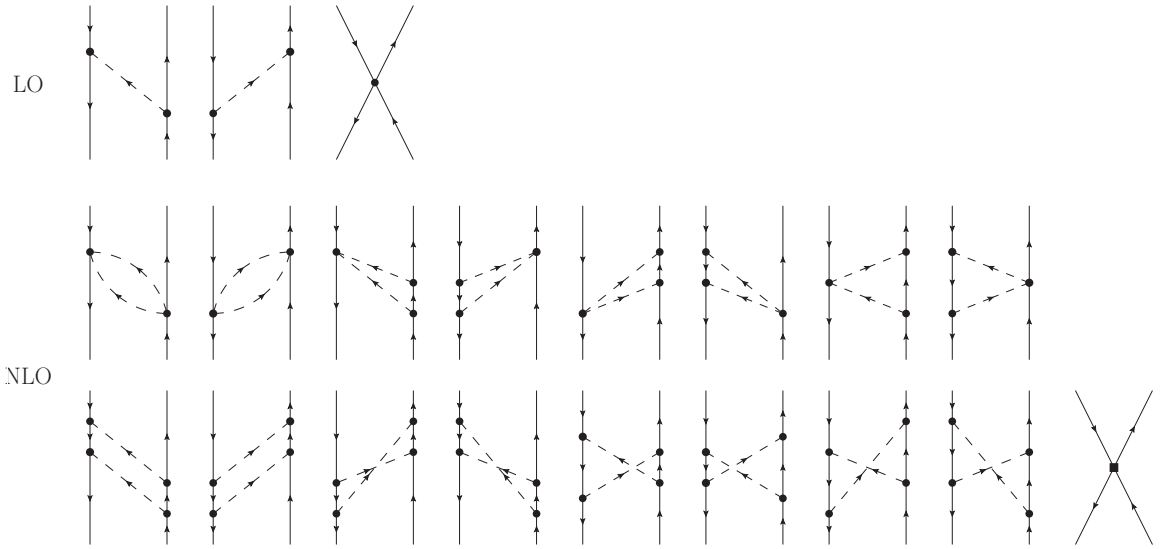

Figure 10. The Feynman diagram for $\bar{N}N$ scattering up to NLO.

The OBE potential for the process of $\bar{p}p \to \bar{p}p$ is defined as

$$\langle \bar{p}p|W_{BB\Phi}GW_{BB\Phi}|\bar{p}p\rangle = \frac{1}{(2\pi)^3}\delta^3(\boldsymbol{p}_1+\boldsymbol{p}_2-\boldsymbol{p}_1'-\boldsymbol{p}_2')V^{\rm OBE}_{\bar{p}p\to\bar{p}p}\,, \tag{A.8}$$

where the propagator is $G = 1/(z - H_0 + i0^+)$, with H_0 the energy operator of the free particle and z the total energy of the initial state. $\boldsymbol{p}_{1,2}$ is the three-momentum of the proton, antiproton in the initial state, and $\boldsymbol{p}'_{1,2}$ for the final state. In the language of creation and annihilation operators, the initial and final states are defined as

$$|\bar{p}p\rangle = d^\dagger_{\boldsymbol{p}_1,\lambda_1}c^\dagger_{\boldsymbol{p}_2,\lambda_2}|0\rangle, \quad \langle\bar{p}p| = \langle 0|c_{\boldsymbol{p}_1',\lambda_1'}d_{\boldsymbol{p}_2',\lambda_2'}\,, \tag{A.9}$$

where $\lambda_i^{(\prime)}$ $(i = 1, 2)$ is the helicity of the proton or antiproton in initial (final) states. The potential in eq. (A.8) includes π^0 and η exchanges. Taking π^0 exchange as an example, the Lagrangian $-f_{NN\pi}\bar{p}\gamma^\mu\gamma^5 p\partial_\mu\pi^0$ in eq. (A.4) needs to be considered. The proton, antiproton and π^0 fields are defined as

$$\begin{aligned}
\bar{p} &= \frac{1}{(2\pi)^{3/2}}\sum_\xi\int \mathrm{d}^3\boldsymbol{k}\left[\bar{u}(\boldsymbol{k},\xi)c^\dagger_{\boldsymbol{k}\xi}e^{ik\cdot x}+\bar{v}(\boldsymbol{k},\xi)d_{\boldsymbol{k}\xi}e^{-ik\cdot x}\right],\\
p &= \frac{1}{(2\pi)^{3/2}}\sum_\xi\int \mathrm{d}^3\boldsymbol{k}\left[u(\boldsymbol{k},\xi)c_{\boldsymbol{k}\xi}e^{-ik\cdot x}+v(\boldsymbol{k},\xi)d^\dagger_{\boldsymbol{k}\xi}e^{ik\cdot x}\right],\\
\pi^0 &= \frac{1}{(2\pi)^{3/2}}\int\frac{\mathrm{d}^3\boldsymbol{l}}{\sqrt{2\omega_{l,\pi}}}\left(a^0_{\boldsymbol{l}}e^{-il\cdot x}+a^{0\dagger}_{\boldsymbol{l}}e^{il\cdot x}\right),
\end{aligned} \tag{A.10}$$

where the pion energy is $\omega_{l,\pi} = \sqrt{l^2+m_\pi^2}$, with $l = |\boldsymbol{l}|$. The creation and annihilation operators of the proton and antiproton, $c^\dagger_{\boldsymbol{k}\xi}, d^\dagger_{\boldsymbol{k}\xi}$ and $c_{\boldsymbol{k}\xi}, d_{\boldsymbol{k}\xi}$, satisfy anticommutation relations, and the pion operators, $a^{0\dagger}_{\boldsymbol{l}}$ and $a^0_{\boldsymbol{l}}$ of π^0, satisfy commutation relations. The spinors of the proton and the antiproton are given as

$$u(\boldsymbol{k},\xi) = \sqrt{\frac{E_k+M_N}{2E_k}}\begin{pmatrix}1\\ \frac{\boldsymbol{\sigma}\cdot\boldsymbol{k}}{E_k+M_N}\end{pmatrix}|\xi\rangle, \quad v(\boldsymbol{k},\xi) = i\gamma^2u^*(\boldsymbol{p},\xi)\,, \tag{A.11}$$

JHEP08(2024)208

with the energy $E_k = \sqrt{k^2 + M_N^2}$ and $k = |\boldsymbol{k}|$. Applying eqs. (A.9), (A.10) and the commutation and anticommutation relations between the creation and annihilation operators, the π^0 exchange potential $V^{\pi^0}_{\bar{p}p\to\bar{p}p}$ for $\bar{p}p$ scattering can be obtained. One has

$$V^{\pi^0}_{\bar{p}p\to\bar{p}p} = f^2_{NN\pi}\left[-\frac{\bar{u}(\boldsymbol{p}_2',\lambda_2')\not{l}\gamma^5 u(\boldsymbol{p}_2,\lambda_2)\bar{v}(\boldsymbol{p}_1,\lambda_1)\not{l}\gamma^5 v(\boldsymbol{p}_1',\lambda_1')}{2\omega_{|\boldsymbol{p}_1'-\boldsymbol{p}_1|,\pi}(z - E_{p_2} - E_{p_1'} - \omega_{|\boldsymbol{p}_1'-\boldsymbol{p}_1|,\pi})}\right.$$
$$\left.-\frac{\bar{v}(\boldsymbol{p}_1,\lambda_1)\not{l}'\gamma^5 v(\boldsymbol{p}_1',\lambda_1')\bar{u}(\boldsymbol{p}_2',\lambda_2')\not{l}'\gamma^5 u(\boldsymbol{p}_2,\lambda_2)}{2\omega_{|\boldsymbol{p}_1'-\boldsymbol{p}_1|,\pi}(z - E_{p_1} - E_{p_2'} - \omega_{|\boldsymbol{p}_1'-\boldsymbol{p}_1|,\pi})}\right] + \cdots, \tag{A.12}$$

where $\cdots$ denotes the s channel contribution caused by $\bar{N}N$ annihilating into a pion and then creating a $\bar{N}N$ pair. This part is not written out as it will be absorbed into the annihilation potential eventually. The corresponding Feynman diagrams are shown in the first row of figure 10, the first term corresponds to the second diagram, with the momentum of π^0 given by $l^\mu = (\omega_{|\boldsymbol{p}_1'-\boldsymbol{p}_1|,\pi}, -\boldsymbol{p}_1' + \boldsymbol{p}_1)$, and the second term corresponds to the first diagram, with $l'^\mu = (\omega_{|\boldsymbol{p}_1'-\boldsymbol{p}_1|,\pi}, \boldsymbol{p}_1' - \boldsymbol{p}_1)$. According to eq. (A.11), the relation between the u and v spinors can be obtained through transposition and Dirac matrix operation

$$\bar{v}\gamma^\mu\gamma^5 v = -\bar{u}\gamma^\mu\gamma^5 u\,. \tag{A.13}$$

Transforming the terms in eq. (A.12) into the c.m.f. and applying eq. (A.13), the potential $V^{\pi^0}_{\bar{p}p\to\bar{p}p}$ is finally given as

$$V^{\pi^0}_{\bar{p}p\to\bar{p}p} = f^2_{NN\pi}\left[\frac{\bar{u}(-\boldsymbol{p}',\lambda_2')\not{l}\gamma^5 u(-\boldsymbol{p},\lambda_2)\bar{u}(\boldsymbol{p}',\lambda_1')\not{l}\gamma^5 u(\boldsymbol{p},\lambda_1)}{2\omega_{q,\pi}(z - E_p - E_{p'} - \omega_{q,\pi})}\right.$$
$$\left.+\frac{\bar{u}(\boldsymbol{p}',\lambda_1')\not{l}'\gamma^5 u(\boldsymbol{p},\lambda_1)\bar{u}(-\boldsymbol{p}',\lambda_2')\not{l}'\gamma^5 u(-\boldsymbol{p},\lambda_2)}{2\omega_{q,\pi}(z - E_p - E_{p'} - \omega_{q,\pi})}\right], \tag{A.14}$$

where $\boldsymbol{p}$ and $\boldsymbol{p}'$ are the three-momenta of the initial and final states in the c.m.f., respectively. Note that in the c.m.f., the momenta of the π^0 becomes $l^\mu = (\omega_{q,\pi}, -\boldsymbol{q})$ and $l'^\mu = (\omega_{q,\pi}, \boldsymbol{q})$ for these two terms, where the transferred momentum is $\boldsymbol{q} = \boldsymbol{p}' - \boldsymbol{p}$. In the non-relativistic approximation the terms involving the spinors of eq. (A.11) reduce to

$$\bar{u}(\boldsymbol{p}',\lambda')\not{l}\gamma^5 u(\boldsymbol{p},\lambda) \approx \langle\lambda'|\boldsymbol{\sigma}\cdot\boldsymbol{q}|\lambda\rangle, \quad \bar{u}(\boldsymbol{p}',\lambda')\not{l}'\gamma^5 u(\boldsymbol{p},\lambda) \approx -\langle\lambda'|\boldsymbol{\sigma}\cdot\boldsymbol{q}|\lambda\rangle. \tag{A.15}$$

Adopting the static approximation for z in the propagator yields $z \simeq E_p + E_{p'}$ [66]. Combining it with eq. (A.15), one obtains the final form of the one-pion exchange potential,

$$V^{\pi^0}_{\bar{p}p\to\bar{p}p} \approx -f^2_{NN\pi}\frac{\langle\lambda_2'|\boldsymbol{\sigma}\cdot\boldsymbol{q}|\lambda_2\rangle\langle\lambda_1'|\boldsymbol{\sigma}\cdot\boldsymbol{q}|\lambda_1\rangle}{\boldsymbol{q}^2 + m_\pi^2}\,. \tag{A.16}$$

Similarly, the OBE potential for the $\bar{p}p$ scattering from η exchange has the following form

$$V^{\eta}_{\bar{p}p\to\bar{p}p} \approx -f^2_{NN\eta}\frac{\langle\lambda_2'|\boldsymbol{\sigma}\cdot\boldsymbol{q}|\lambda_2\rangle\langle\lambda_1'|\boldsymbol{\sigma}\cdot\boldsymbol{q}|\lambda_1\rangle}{\boldsymbol{q}^2 + m_\eta^2}\,. \tag{A.17}$$

As mentioned above, the potential for the process $\bar{p}p \to \bar{n}n$ is also needed to determine the $\bar{N}N$ potential in the isospin basis. One has

$$\langle\bar{n}n|W_{BB\Phi}GW_{BB\Phi}|\bar{p}p\rangle = \frac{1}{(2\pi)^3}\delta^3(\boldsymbol{p}_1 + \boldsymbol{p}_2 - \boldsymbol{p}_1' - \boldsymbol{p}_2')V^{\rm OBE}_{\bar{p}p\to\bar{n}n}\,. \tag{A.18}$$

JHEP08(2024)208

Isospin	π	η
$I=0$	3	1
$I=1$	-1	1

Table 4. The isospin factor $\mathcal{I}_{\bar{N}N\to\bar{N}N}$ for the OBE potentials.

Here, only π exchange appears. The relevant Lagrangians are $-f_{NN\pi}\sqrt{2}\bar{p}\gamma^\mu\gamma^5 n\partial_\mu\pi^+$ and $-f_{NN\pi}\sqrt{2}\bar{n}\gamma^\mu\gamma^5 p\partial_\mu\pi^-$ from $\mathcal{L}_{BB\Phi}$. With a calculation similar to the one above one obtains

$$V^{\rm OBE}_{\bar{\rm p}{\rm p}\to\bar{\rm n}{\rm n}} = -2f^2_{NN\pi}\frac{\langle\lambda_2'|\boldsymbol{\sigma}\cdot\boldsymbol{q}|\lambda_2\rangle\langle\lambda_1'|\boldsymbol{\sigma}\cdot\boldsymbol{q}|\lambda_1\rangle}{\boldsymbol{q}^2+m_\pi^2}\,. \tag{A.19}$$

Finally, the potential in the isospin basis can be obtained through the relation given in eq. (A.7),

$$\begin{aligned} V^{I=0}_{\bar{N}N} &= -3f^2_{NN\pi}\frac{\langle\lambda_2'|\boldsymbol{\sigma}\cdot\boldsymbol{q}|\lambda_2\rangle\langle\lambda_1'|\boldsymbol{\sigma}\cdot\boldsymbol{q}|\lambda_1\rangle}{\boldsymbol{q}^2+m_\pi^2} - f^2_{NN\eta}\frac{\langle\lambda_2'|\boldsymbol{\sigma}\cdot\boldsymbol{q}|\lambda_2\rangle\langle\lambda_1'|\boldsymbol{\sigma}\cdot\boldsymbol{q}|\lambda_1\rangle}{\boldsymbol{q}^2+m_\eta^2}\,,\\ V^{I=1}_{\bar{N}N} &= f^2_{NN\pi}\frac{\langle\lambda_2'|\boldsymbol{\sigma}\cdot\boldsymbol{q}|\lambda_2\rangle\langle\lambda_1'|\boldsymbol{\sigma}\cdot\boldsymbol{q}|\lambda_1\rangle}{\boldsymbol{q}^2+m_\pi^2} - f^2_{NN\eta}\frac{\langle\lambda_2'|\boldsymbol{\sigma}\cdot\boldsymbol{q}|\lambda_2\rangle\langle\lambda_1'|\boldsymbol{\sigma}\cdot\boldsymbol{q}|\lambda_1\rangle}{\boldsymbol{q}^2+m_\eta^2}\,. \end{aligned} \tag{A.20}$$

Defining an isospin factor $\mathcal{I}_{\bar{N}N\to\bar{N}N}$, similar to ref. [54], the final results of OBE can be expressed as

$$V^{\rm OBE}_{\bar{N}N\to\bar{N}N} = -f^2_{NNP}\frac{\langle\lambda_2'|\boldsymbol{\sigma}\cdot\boldsymbol{q}|\lambda_2\rangle\langle\lambda_1'|\boldsymbol{\sigma}\cdot\boldsymbol{q}|\lambda_1\rangle}{\boldsymbol{q}^2+m_P^2}\mathcal{I}_{\bar{N}N\to\bar{N}N}\,, \tag{A.21}$$

with P the relevant pseudoscalar meson. The isospin factors can be extracted from the potentials as given in eq. (A.20), and they are listed in table 4. Comparing them with the isospin factors of the OBE potential of NN, as shown in table 2 of ref. [54], one finds signs as expected from the G-parity transformation, eq. (2.7). The relativistic correction is considered in OBE potential, that is

$$\tilde{V}^{\rm OBE}_{\bar{N}N\to\bar{N}N} = V^{\rm OBE}_{\bar{N}N\to\bar{N}N}\left(1-\frac{p'^2+p^2}{2m_N^2}\right) \tag{A.22}$$

A.3 The TBE potential

The TBE potentials correspond to the set of one-loop Feynman diagrams shown in the second and third rows in figure 10. As discussed above, the potentials will be taken as kernel in the LS equation to obtain the $\bar{N}N$ scattering amplitudes. Therefore, to avoid double counting, we should consider only the irreducible part of those diagrams. In this section, we take the football diagrams as an example to illustrate the calculation of TBE potentials. The corresponding Feynman diagrams are the first two graphs in the second row of figure 10. The potential for the process $\bar{p}p\to\bar{p}p$ is defined as

$$\langle\bar{p}p|W_{BB\Phi\Phi}GW_{BB\Phi\Phi}|\bar{p}p\rangle = \frac{1}{(2\pi)^3}\delta^3(\boldsymbol{p}_1+\boldsymbol{p}_2-\boldsymbol{p}_1'-\boldsymbol{p}_2')V^{\rm Football}_{\bar{p}p\to\bar{p}p}\,, \tag{A.23}$$

JHEP08(2024)208

where the potential $V^{\rm Football}_{\bar{p}p\to\bar{p}p}$ contains $\pi^+\pi^-$, K^+K^- and $K^0\bar{K}^0$ exchanges. For $\pi^+\pi^-$ exchange, the vertex is coming from the chiral effective Lagrangian $i\bar{p}\gamma^\mu p(\pi^+\partial_\mu\pi^- - \pi^-\partial_\mu\pi^+)/4f_0^2$. The π^+ and π^- meson fields are defined as

$$\begin{aligned}\pi^+ &= \frac{1}{(2\pi)^{3/2}}\int\frac{\mathrm{d}^3\boldsymbol{l}}{\sqrt{2\omega_{l,\pi}}}\left(a_{\boldsymbol{l}}e^{-il\cdot x}+b^\dagger_{\boldsymbol{l}}e^{il\cdot x}\right),\\ \pi^- &= \frac{1}{(2\pi)^{3/2}}\int\frac{\mathrm{d}^3\boldsymbol{l}}{\sqrt{2\omega_{l,\pi}}}\left(b_{\boldsymbol{l}}e^{-il\cdot x}+a^\dagger_{\boldsymbol{l}}e^{il\cdot x}\right),\end{aligned}\tag{A.24}$$

where $a^\dagger_{\boldsymbol{l}}, a_{\boldsymbol{l}}$ and $b^\dagger_{\boldsymbol{l}}, b_{\boldsymbol{l}}$ are the creation and annihilation operators of π^+ and π^-, respectively. After performing commutation and anti-commutation operations between the creation and annihilation operators for mesons and baryons, eliminating the Dirac delta function through momentum integration, and summing the spins, one has

$$\begin{aligned}V^{\pi^+\pi^-}_{\bar{p}p\to\bar{p}p} = &-\frac{1}{16f_0^4}\int\frac{\mathrm{d}^3\boldsymbol{l}_1}{(2\pi)^3}\left[\frac{\bar{u}(\boldsymbol{p}_2',\lambda_2')(\not{l}_1-\not{l}_2)u(\boldsymbol{p}_2,\lambda_2)\bar{v}(\boldsymbol{p}_1,\lambda_1)(\not{l}_1-\not{l}_2)v(\boldsymbol{p}_1',\lambda_1')}{4\omega_{l_1,\pi}\omega_{|\boldsymbol{l}_1+\boldsymbol{p}_1'-\boldsymbol{p}_1|,\pi}(z-E_{p_2}-E_{p_1'}-\omega_{l_1,\pi}-\omega_{|\boldsymbol{l}_1+\boldsymbol{p}_1'-\boldsymbol{p}_1|,\pi})}\right.\\ &\left.+\frac{\bar{v}(\boldsymbol{p}_1,\lambda_1)(\not{l}_1-\not{l}_2')v(\boldsymbol{p}_1',\lambda_1')\bar{u}(\boldsymbol{p}_2',\lambda_2')(\not{l}_1-\not{l}_2')u(\boldsymbol{p}_2,\lambda_2)}{4\omega_{l_1,\pi}\omega_{|\boldsymbol{l}_1-\boldsymbol{p}_1'+\boldsymbol{p}_1|,\pi}(z-E_{p_1}-E_{p_2'}-\omega_{l_1,\pi}-\omega_{|\boldsymbol{l}_1-\boldsymbol{p}_1'+\boldsymbol{p}_1|,\pi})}\right]+\cdots,\end{aligned}\tag{A.25}$$

where $\cdots$ denotes the s channel contributions again. Specifically, the first diagram in the second row of figure 10 corresponds to the second term of eq. (A.25), while the second diagram corresponds to the first term. The four-momenta of pions in the first term are $l_1^\mu=(\omega_{l_1,\pi},\boldsymbol{l}_1)$ for the π^+ and $l_2^\mu=(\omega_{|\boldsymbol{l}_1+\boldsymbol{p}_1'-\boldsymbol{p}_1|,\pi},-\boldsymbol{l}_1-\boldsymbol{p}_1'+\boldsymbol{p}_1)$ for the π^-, and the momenta in the second term are l_1 for the π^+ and $l_2'^\mu=(\omega_{|\boldsymbol{l}_1-\boldsymbol{p}_1'+\boldsymbol{p}_1|,\pi},-\boldsymbol{l}_1+\boldsymbol{p}_1'-\boldsymbol{p}_1)$ for the π^-. One useful relation for transforming the Lorentz vectors composed of spinors and Dirac matrix is

$$\bar{v}\gamma^\mu v=\bar{u}\gamma^\mu u\,.\tag{A.26}$$

With it, one can transform the potentials given in eq. (A.25) into the c.m.f.,

$$\begin{aligned}V^{\pi^+\pi^-}_{\bar{p}p\to\bar{p}p} = &-\frac{1}{16f_0^4}\int\frac{\mathrm{d}^3\boldsymbol{l}_1}{(2\pi)^3}\left[\frac{\bar{u}(-\boldsymbol{p}',\lambda_2')(\not{l}_1-\not{l}_2)u(-\boldsymbol{p},\lambda_2)\bar{u}(\boldsymbol{p}',\lambda_1')(\not{l}_1-\not{l}_2)u(\boldsymbol{p},\lambda_1)}{4\omega_{l_1,\pi}\omega_{|\boldsymbol{l}_1+\boldsymbol{q}|,\pi}(z-E_{p_2}-E_{p_1'}-\omega_{l_1,\pi}-\omega_{|\boldsymbol{l}_1+\boldsymbol{q}|,\pi})}\right.\\ &\left.+\frac{\bar{u}(\boldsymbol{p}',\lambda_1')(\not{l}_1-\not{l}_2')u(\boldsymbol{p},\lambda_1)\bar{u}(-\boldsymbol{p}',\lambda_2')(\not{l}_1-\not{l}_2')u(-\boldsymbol{p},\lambda_2)}{4\omega_{l_1,\pi}\omega_{|\boldsymbol{l}_1-\boldsymbol{q}|,\pi}(z-E_{p_1}-E_{p_2'}-\omega_{l_1,\pi}-\omega_{|\boldsymbol{l}_1-\boldsymbol{q}|,\pi})}\right]+\cdots,\end{aligned}\tag{A.27}$$

where $l_2^\mu=(\omega_{|\boldsymbol{l}_1+\boldsymbol{q}|,\pi},-\boldsymbol{l}_1-\boldsymbol{q})$ and $l_2'^\mu=(\omega_{|\boldsymbol{l}_1-\boldsymbol{q}|,\pi},-\boldsymbol{l}_1+\boldsymbol{q})$. For the spinor part in non-relativistic approximation one obtains

$$\begin{aligned}\bar{u}(\boldsymbol{p}',\lambda')(\not{l}_1-\not{l}_2)u(\boldsymbol{p},\lambda)&\approx\langle\lambda'|\lambda\rangle(\omega_{l_1,\pi}-\omega_{|\boldsymbol{l}_1+\boldsymbol{q}|,\pi}),\\ \bar{u}(\boldsymbol{p}',\lambda')(\not{l}_1-\not{l}_2')u(\boldsymbol{p},\lambda)&\approx\langle\lambda'|\lambda\rangle(\omega_{l_1,\pi}-\omega_{|\boldsymbol{l}_1-\boldsymbol{q}|,\pi}).\end{aligned}\tag{A.28}$$

JHEP08(2024)208

Then, the potential can be written in the form

$$
\begin{aligned}
V^{\pi^+\pi^-}_{\bar{p}p\to\bar{p}p} \approx & \frac{1}{16f_0^4}\int\frac{\mathrm{d}^3\boldsymbol{l}_1}{(2\pi)^3}\left[\frac{\langle\lambda_2'|\lambda_2\rangle\langle\lambda_1'|\lambda_1\rangle(\omega_{l_1,\pi}-\omega_{|\boldsymbol{l}_1+\boldsymbol{q}|,\pi})^2}{4\omega_{l_1,\pi}\omega_{|\boldsymbol{l}_1+\boldsymbol{q}|,\pi}(\omega_{l_1,\pi}+\omega_{|\boldsymbol{l}_1+\boldsymbol{q}|,\pi})}\right.\\
&\left.+\frac{\langle\lambda_2'|\lambda_2\rangle\langle\lambda_1'|\lambda_1\rangle(\omega_{l_1,\pi}-\omega_{|\boldsymbol{l}_1-\boldsymbol{q}|,\pi})^2}{4\omega_{l_1,\pi}\omega_{|\boldsymbol{l}_1-\boldsymbol{q}|,\pi}(\omega_{l_1,\pi}+\omega_{|\boldsymbol{l}_1-\boldsymbol{q}|,\pi})}\right]\\
=&\frac{1}{32f_0^4}\int\frac{\mathrm{d}^3\boldsymbol{l}_1}{(2\pi)^3}\frac{\langle\lambda_2'|\lambda_2\rangle\langle\lambda_1'|\lambda_1\rangle(\omega_{l_1,\pi}-\omega_{|\boldsymbol{l}_1+\boldsymbol{q}|,\pi})^2}{\omega_{l_1,\pi}\omega_{|\boldsymbol{l}_1+\boldsymbol{q}|,\pi}(\omega_{l_1,\pi}+\omega_{|\boldsymbol{l}_1+\boldsymbol{q}|,\pi})}\\
=&\frac{1}{32f_0^4}\int\frac{\mathrm{d}^3\boldsymbol{l}_1}{(2\pi)^3}\frac{\langle\lambda_2'|\lambda_2\rangle\langle\lambda_1'|\lambda_1\rangle(\omega_{|\boldsymbol{l}_1-\boldsymbol{q}/2|,\pi}-\omega_{|\boldsymbol{l}_1+\boldsymbol{q}/2|,\pi})^2}{\omega_{|\boldsymbol{l}_1-\boldsymbol{q}/2|,\pi}\omega_{|\boldsymbol{l}_1+\boldsymbol{q}/2|,\pi}(\omega_{|\boldsymbol{l}_1-\boldsymbol{q}/2|,\pi}+\omega_{|\boldsymbol{l}_1+\boldsymbol{q}/2|,\pi})}\\
=&\frac{1}{32f_0^4}\int\frac{\mathrm{d}^3\boldsymbol{l}_1}{8(2\pi)^3}\frac{\langle\lambda_2'|\lambda_2\rangle\langle\lambda_1'|\lambda_1\rangle(\omega_{|\boldsymbol{l}_1/2-\boldsymbol{q}/2|,\pi}-\omega_{|\boldsymbol{l}_1/2+\boldsymbol{q}/2|,\pi})^2}{\omega_{|\boldsymbol{l}_1/2-\boldsymbol{q}/2|,\pi}\omega_{|\boldsymbol{l}_1/2+\boldsymbol{q}/2|,\pi}(\omega_{|\boldsymbol{l}_1/2-\boldsymbol{q}/2|,\pi}+\omega_{|\boldsymbol{l}_1/2+\boldsymbol{q}/2|,\pi})}\\
=&\frac{1}{128f_0^4}\int\frac{\mathrm{d}^3\boldsymbol{l}_1}{(2\pi)^3}\frac{\langle\lambda_2'|\lambda_2\rangle\langle\lambda_1'|\lambda_1\rangle(\omega_{-,\pi}-\omega_{+,\pi})^2}{\omega_{-,\pi}\omega_{+,\pi}(\omega_{-,\pi}+\omega_{+,\pi})}\,,
\end{aligned}
\tag{A.29}
$$

where one has

$$
\omega_{\pm,P}=\sqrt{(\boldsymbol{l}_1\pm\boldsymbol{q})^2+4m_P^2}=2\omega_{|\boldsymbol{l}_1/2\pm\boldsymbol{q}/2|,P}\,. \tag{A.30}
$$

In the first, second, and third steps, one performs the reflection $\boldsymbol{l}_1\to-\boldsymbol{l}_1$, translation $\boldsymbol{l}_1\to\boldsymbol{l}_1-\boldsymbol{q}/2$, and the scaling $\boldsymbol{l}_1\to\boldsymbol{l}_1/2$, respectively.

The football diagrams due to K^+K^- and $K^0\bar{K}^0$ exchanges involve the Lagrangians $i\bar{p}\gamma^\mu p(K^+\partial_\mu K^- - K^-\partial_\mu K^+)/2f_0^2$ and $i\bar{p}\gamma^\mu p(K^0\partial_\mu\bar{K}^0-\bar{K}^0\partial_\mu K^0)/4f_0^2$. Analogous to what has been done for the two pions exchange abovve, one has

$$
\begin{aligned}
V^{K^+K^-}_{\bar{p}p\to\bar{p}p}&=\frac{1}{32f_0^4}\int\frac{\mathrm{d}^3\boldsymbol{l}_1}{(2\pi)^3}\frac{\langle\lambda_2'|\lambda_2\rangle\langle\lambda_1'|\lambda_1\rangle(\omega_{-,K}-\omega_{+,K})^2}{\omega_{-,K}\omega_{+,K}(\omega_{-,K}+\omega_{+,K})}\,,\\
V^{K^0\bar{K}^0}_{\bar{p}p\to\bar{p}p}&=\frac{1}{4}V^{K^+K^-}_{\bar{p}p\to\bar{p}p}\,.
\end{aligned}
\tag{A.31}
$$

At last, one obtains the complete potential of the process of $\bar{p}p\to\bar{p}p$ from the football diagrams,

$$
\begin{aligned}
V^{\text{Football}}_{\bar{p}p\to\bar{p}p}=&\frac{1}{128f_0^4}\int\frac{\mathrm{d}^3\boldsymbol{l}_1}{(2\pi)^3}\frac{\langle\lambda_2'|\lambda_2\rangle\langle\lambda_1'|\lambda_1\rangle(\omega_{-,\pi}-\omega_{+,\pi})^2}{\omega_{-,\pi}\omega_{+,\pi}(\omega_{-,\pi}+\omega_{+,\pi})}\\
&+\frac{5}{128f_0^4}\int\frac{\mathrm{d}^3\boldsymbol{l}_1}{(2\pi)^3}\frac{\langle\lambda_2'|\lambda_2\rangle\langle\lambda_1'|\lambda_1\rangle(\omega_{-,K}-\omega_{+,K})^2}{\omega_{-,K}\omega_{+,K}(\omega_{-,K}+\omega_{+,K})}\,.
\end{aligned}
\tag{A.32}
$$

Similarly, the complete potential of the process of $\bar{p}p\to\bar{n}n$, from the football diagrams with $\pi\pi$ and $K\bar{K}$ exchanges, are given by

$$
\begin{aligned}
V^{\text{Football}}_{\bar{p}p\to\bar{n}n}=&\frac{1}{64f_0^4}\int\frac{\mathrm{d}^3\boldsymbol{l}_1}{(2\pi)^3}\frac{\langle\lambda_2'|\lambda_2\rangle\langle\lambda_1'|\lambda_1\rangle(\omega_{-,\pi}-\omega_{+,\pi})^2}{\omega_{-,\pi}\omega_{+,\pi}(\omega_{-,\pi}+\omega_{+,\pi})}\\
&+\frac{1}{128f_0^4}\int\frac{\mathrm{d}^3\boldsymbol{l}_1}{(2\pi)^3}\frac{\langle\lambda_2'|\lambda_2\rangle\langle\lambda_1'|\lambda_1\rangle(\omega_{-,K}-\omega_{+,K})^2}{\omega_{-,K}\omega_{+,K}(\omega_{-,K}+\omega_{+,K})}\,.
\end{aligned}
\tag{A.33}
$$

JHEP08(2024)208

With eqs. (A.32), (A.33), one gets the potentials of the football diagrams in the isospin basis,

$$
\begin{aligned}
V_{\bar{N}N}^{I=0} &= \frac{3}{128 f_0^4} \int \frac{\mathrm{d}^3 \boldsymbol{l}_1}{(2\pi)^3} \frac{\langle \lambda_2' | \lambda_2 \rangle \langle \lambda_1' | \lambda_1 \rangle (\omega_{-,\pi} - \omega_{+,\pi})^2}{\omega_{-,\pi} \omega_{+,\pi} (\omega_{-,\pi} + \omega_{+,\pi})} \\
&\quad + \frac{3}{64 f_0^4} \int \frac{\mathrm{d}^3 \boldsymbol{l}_1}{(2\pi)^3} \frac{\langle \lambda_2' | \lambda_2 \rangle \langle \lambda_1' | \lambda_1 \rangle (\omega_{-,K} - \omega_{+,K})^2}{\omega_{-,K} \omega_{+,K} (\omega_{-,K} + \omega_{+,K})} , \\
V_{\bar{N}N}^{I=1} &= -\frac{1}{128 f_0^4} \int \frac{\mathrm{d}^3 \boldsymbol{l}_1}{(2\pi)^3} \frac{\langle \lambda_2' | \lambda_2 \rangle \langle \lambda_1' | \lambda_1 \rangle (\omega_{-,\pi} - \omega_{+,\pi})^2}{\omega_{-,\pi} \omega_{+,\pi} (\omega_{-,\pi} + \omega_{+,\pi})} \\
&\quad + \frac{1}{32 f_0^4} \int \frac{\mathrm{d}^3 \boldsymbol{l}_1}{(2\pi)^3} \frac{\langle \lambda_2' | \lambda_2 \rangle \langle \lambda_1' | \lambda_1 \rangle (\omega_{-,K} - \omega_{+,K})^2}{\omega_{-,K} \omega_{+,K} (\omega_{-,K} + \omega_{+,K})} .
\end{aligned}
\tag{A.34}
$$

Again, we can define the isospin factor $\mathcal{I}^{\text{Football}}_{\bar{N}N \to \bar{N}N}$ for simplicity. One has

$$
V_{\bar{N}N}^{\text{Football}} = -\frac{1}{1024 f_0^4} \int \frac{\mathrm{d}^3 \boldsymbol{l}_1'}{(2\pi)^3} \frac{\langle \lambda_2' | \lambda_2 \rangle \langle \lambda_1' | \lambda_1 \rangle (\omega_{+,P} - \omega_{-,P})^2}{\omega_{+,P} \omega_{-,P} (\omega_{+,P} + \omega_{-,P})} \mathcal{I}^{\text{Football}}_{\bar{N}N \to \bar{N}N} . \tag{A.35}
$$

The isospin factors are extracted from eq. (A.34) and listed in table 5. Note that the isospin factors for the planar box, crossed box, left triangle, right triangle diagrams are also listed. A detailed derivation of those contributions can be found in appendix A.5.

Comparing with the isospin factors of the NN potentials given by ref. [54], for π and η we recover again the G-parity transformation, that is,

$$
V_{\bar{N}N}^{\text{TBE}} = (-1)^{I_1 + I_2} V_{NN}^{\text{TBE}} ,
$$

where I_1 and I_2 are the isospin of the two exchanged pseudoscalar bosons. Specifically, for $\pi\eta$ exchanges, the TBE potentials of $\bar{N}N$ and NN scatterings differ by a minus sign, and for $\pi\pi$ and $\eta\eta$ exchanges, they have the same sign.[4] However, this rule is not applicable for $K\bar{K}$ exchange simply because K and $\bar{K}$ do not have definite G-parity.

A.4 The contact terms and the annihilation potential

Besides the contributions from boson exchanges, there are standard contact terms and an annihilation part, too. The contact terms for ${}^3S_1 - {}^3D_1$ partial waves up to NLO are given by [51, 59, 61]

$$
\begin{aligned}
V({}^3S_1) &= \tilde{C}_{{}^3S_1} + C_{{}^3S_1} (p^2 + p'^2) , \\
V({}^3D_1 - {}^3S_1) &= C_{\epsilon_1} p'^2 , \quad V({}^3S_1 - {}^3D_1) = C_{\epsilon_1} p^2 ,
\end{aligned}
\tag{A.36}
$$

where p and p' are the c.m.f. momenta of the initial and final $\bar{N}N$ systems, respectively. Here, the $\tilde{C}_i$ denote the LECs that arise at leading order (LO), corresponding to the contact terms without derivatives. The C_i arise at NLO, corresponding to the terms with two derivatives. An essential difference between the NN and $\bar{N}N$ interaction is the presence of annihilation processes in the latter. Following refs. [59, 61], the annihilation part of the $\bar{N}N$ potential

[4] It is worth pointing out that these relations have already been given in ref. [47], too.

JHEP08(2024)208

	Isospin	Intermediate baryons	$\pi\pi$	$\pi\eta$	$\eta\eta$	$K\bar{K}$
Football	$I=0$		-24	–	–	-48
	$I=1$		8	–	–	-32
Left Triangle	$I=0$	N	12	–	–	–
		Λ	–	–	–	6
		Σ	–	–	–	6
	$I=1$	N	-4	–	–	–
		Λ	–	–	–	2
		Σ	–	–	–	10
Right Triangle	$I=0$	$\bar{N}$	12	–	–	–
		$\bar{\Lambda}$	–	–	–	6
		$\bar{\Sigma}$	–	–	–	6
	$I=1$	$\bar{N}$	-4	–	–	–
		$\bar{\Lambda}$	–	–	–	2
		$\bar{\Sigma}$	–	–	–	10
Planar Box	$I=0$	$\bar{N}N$	9	6	1	–
		$\bar{\Lambda}\Lambda$	–	–	–	2
		$\bar{\Sigma}\Sigma$	–	–	–	6
		$\bar{\Sigma}\Lambda+\bar{\Lambda}\Sigma$	–	–	–	0
	$I=1$	$\bar{N}N$	1	-2	1	–
		$\bar{\Lambda}\Lambda$	–	–	–	0
		$\bar{\Sigma}\Sigma$	–	–	–	4
		$\bar{\Sigma}\Lambda+\bar{\Lambda}\Sigma$	–	–	–	4
Cross Box	$I=0$	$\bar{N}N$	-3	6	1	–
		$\bar{\Lambda}\Lambda$	–	–	–	0
		$\bar{\Sigma}\Sigma$	–	–	–	0
		$\bar{\Sigma}\Lambda+\bar{\Lambda}\Sigma$	–	–	–	0
	$I=1$	$\bar{N}N$	5	-2	1	–
		$\bar{\Lambda}\Lambda$	–	–	–	0
		$\bar{\Sigma}\Sigma$	–	–	–	0
		$\bar{\Sigma}\Lambda+\bar{\Lambda}\Sigma$	–	–	–	0

Table 5. Isospin factors of TBE potentials for $\bar{N}N$ scattering.

for the coupled ${}^3S_1 - {}^3D_1$ partial wave is parameterized as

$$\begin{aligned}
V^{\rm ann}({}^3S_1) &= -i(\tilde{C}^a_{{}^3S_1} + C^a_{{}^3S_1} p^2)(\tilde{C}^a_{{}^3S_1} + C^a_{{}^3S_1} p'^2)\,, \\
V^{\rm ann}({}^3D_1 - {}^3S_1) &= -iC^a_{\epsilon_1} p'^2(\tilde{C}^a_{{}^3S_1} + C^a_{{}^3S_1} p^2)\,, \\
V^{\rm ann}({}^3S_1 - {}^3D_1) &= -iC^a_{\epsilon_1} p^2(\tilde{C}^a_{{}^3S_1} + C^a_{{}^3S_1} p'^2)\,, \\
V^{\rm ann}({}^3D_1) &= -i[(C^a_{\epsilon_1})^2 + (C^a_{{}^3D_1})^2] p^2 p'^2\,,
\end{aligned} \tag{A.37}$$

which is consistent with requirements from unitarity. In the expressions above, the parameters $\tilde{C}^a$ and C^a are real. All the potentials used in the LS equation are cut off by a regulator

JHEP08(2024)208

function, $f_R(\Lambda) = \exp[-(p^6 + p'^6)/\Lambda^6]$, to suppress high-momentum components [38, 54]. To explore the dependence of our results on the cutoff, we consider a range of cut-off values: Λ =750, 800, 850, 900, 950 MeV. These values are noticeably larger than the ones required and used in standard χEFT calculations [51, 61], but reflect the fact that we want to apply our $\bar{N}N$ interaction over an extended energy range.

A.5 The results of all the TBE potentials

In section A.3, the calculation of the football diagram is described. In this section, the potentials due to the triangle, planar box, and cross box diagrams will be given. The triangle diagrams refer to the left triangle and right triangle diagrams. For the left triangle diagrams in the physical basis, one has

$$
\begin{aligned}
V^{\rm LeftTriangle}_{\bar{\rm n}{\rm n}\to\bar{\rm n}{\rm n}} &= V^{\rm LeftTriangle}_{\bar{\rm p}{\rm p}\to\bar{\rm p}{\rm p}} \\
&= -\frac{f^2_{NN\pi}}{8f_0^2}\int\frac{{\rm d}^3\boldsymbol{l}_1}{(2\pi)^3}\frac{(\boldsymbol{l}_1^2-\boldsymbol{q}^2)\langle\lambda_2'|\lambda_2\rangle\langle\lambda_1'|\lambda_1\rangle}{\omega_{+,\pi}\omega_{-,\pi}(\omega_{+,\pi}+\omega_{-,\pi})} - \frac{f^2_{\Lambda NK}}{8f_0^2}\int\frac{{\rm d}^3\boldsymbol{l}_1}{(2\pi)^3}\frac{(\boldsymbol{l}_1^2-\boldsymbol{q}^2)\langle\lambda_2'|\lambda_2\rangle\langle\lambda_1'|\lambda_1\rangle}{\omega_{+,K}\omega_{-,K}(\omega_{+,K}+\omega_{-,K})} \\
&\quad - \frac{f^2_{\Sigma NK}}{4f_0^2}\int\frac{{\rm d}^3\boldsymbol{l}_1}{(2\pi)^3}\frac{(\boldsymbol{l}_1^2-\boldsymbol{q}^2)\langle\lambda_2'|\lambda_2\rangle\langle\lambda_1'|\lambda_1\rangle}{\omega_{+,K}\omega_{-,K}(\omega_{+,K}+\omega_{-,K})}, \\
V^{\rm LeftTriangle}_{\bar{\rm p}{\rm p}\to\bar{\rm n}{\rm n}} &= -\frac{f^2_{NN\pi}}{4f_0^2}\int\frac{{\rm d}^3\boldsymbol{l}_1}{(2\pi)^3}\frac{(\boldsymbol{l}_1^2-\boldsymbol{q}^2)\langle\lambda_2'|\lambda_2\rangle\langle\lambda_1'|\lambda_1\rangle}{\omega_{+,\pi}\omega_{-,\pi}(\omega_{+,\pi}+\omega_{-,\pi})} - \frac{f^2_{\Lambda NK}}{16f_0^2}\int\frac{{\rm d}^3\boldsymbol{l}_1}{(2\pi)^3}\frac{(\boldsymbol{l}_1^2-\boldsymbol{q}^2)\langle\lambda_2'|\lambda_2\rangle\langle\lambda_1'|\lambda_1\rangle}{\omega_{+,K}\omega_{-,K}(\omega_{+,K}+\omega_{-,K})} \\
&\quad + \frac{f^2_{\Sigma NK}}{16f_0^2}\int\frac{{\rm d}^3\boldsymbol{l}_1}{(2\pi)^3}\frac{(\boldsymbol{l}_1^2-\boldsymbol{q}^2)\langle\lambda_2'|\lambda_2\rangle\langle\lambda_1'|\lambda_1\rangle}{\omega_{+,K}\omega_{-,K}(\omega_{+,K}+\omega_{-,K})}.
\end{aligned}
\tag{A.38}
$$

Transforming them into the isospin basis, the potentials are

$$
\begin{aligned}
V^{I=0}_{\bar{N}N} &= -\frac{3f^2_{NN\pi}}{8f_0^2}\int\frac{{\rm d}^3\boldsymbol{l}_1}{(2\pi)^3}\frac{(\boldsymbol{l}_1^2-\boldsymbol{q}^2)\langle\lambda_2'|\lambda_2\rangle\langle\lambda_1'|\lambda_1\rangle}{\omega_{+,\pi}\omega_{-,\pi}(\omega_{+,\pi}+\omega_{-,\pi})} - \frac{3f^2_{\Lambda NK}}{16f_0^2}\int\frac{{\rm d}^3\boldsymbol{l}_1}{(2\pi)^3}\frac{(\boldsymbol{l}_1^2-\boldsymbol{q}^2)\langle\lambda_2'|\lambda_2\rangle\langle\lambda_1'|\lambda_1\rangle}{\omega_{+,K}\omega_{-,K}(\omega_{+,K}+\omega_{-,K})} \\
&\quad - \frac{3f^2_{\Sigma NK}}{16f_0^2}\int\frac{{\rm d}^3\boldsymbol{l}_1}{(2\pi)^3}\frac{(\boldsymbol{l}_1^2-\boldsymbol{q}^2)\langle\lambda_2'|\lambda_2\rangle\langle\lambda_1'|\lambda_1\rangle}{\omega_{+,K}\omega_{-,K}(\omega_{+,K}+\omega_{-,K})}, \\
V^{I=1}_{\bar{N}N} &= \frac{f^2_{NN\pi}}{8f_0^2}\int\frac{{\rm d}^3\boldsymbol{l}_1}{(2\pi)^3}\frac{(\boldsymbol{l}_1^2-\boldsymbol{q}^2)\langle\lambda_2'|\lambda_2\rangle\langle\lambda_1'|\lambda_1\rangle}{\omega_{+,\pi}\omega_{-,\pi}(\omega_{+,\pi}+\omega_{-,\pi})} - \frac{f^2_{\Lambda NK}}{16f_0^2}\int\frac{{\rm d}^3\boldsymbol{l}_1}{(2\pi)^3}\frac{(\boldsymbol{l}_1^2-\boldsymbol{q}^2)\langle\lambda_2'|\lambda_2\rangle\langle\lambda_1'|\lambda_1\rangle}{\omega_{+,K}\omega_{-,K}(\omega_{+,K}+\omega_{-,K})} \\
&\quad - \frac{5f^2_{\Sigma NK}}{16f_0^2}\int\frac{{\rm d}^3\boldsymbol{l}_1}{(2\pi)^3}\frac{(\boldsymbol{l}_1^2-\boldsymbol{q}^2)\langle\lambda_2'|\lambda_2\rangle\langle\lambda_1'|\lambda_1\rangle}{\omega_{+,K}\omega_{-,K}(\omega_{+,K}+\omega_{-,K})}.
\end{aligned}
\tag{A.39}
$$

The isospin factor for the potential due to the left triangle diagram is defined by

$$
V^{\rm LeftTriangle}_{\bar{N}N} = -\frac{f^2_{NB_iP}}{32f_0^2}\int\frac{{\rm d}^3\boldsymbol{l}_1}{(2\pi)^3}\frac{(\boldsymbol{l}_1^2-\boldsymbol{q}^2)\langle\lambda_2'|\lambda_2\rangle\langle\lambda_1'|\lambda_1\rangle}{\omega_{+,P}\omega_{-,P}(\omega_{+,P}+\omega_{-,P})}\mathcal{I}^{\rm LeftTriangle}_{\bar{N}N\to\bar{N}N}, \tag{A.40}
$$

where B_i denotes the intermediate baryon. The interaction potential from the right triangle diagrams are the same as those of the left triangle, in the non-relativistic approximation. The isospin factors are listed in table 5. Comparing with the NN potential given by ref. [54], one sees that the potential due to $\pi\pi$ exchanges satisfies the G-parity transformation rule, as expected, while that for the $K\bar{K}$ exchanges is different.

JHEP08(2024)208

The box diagrams include planar-box and crossed-box diagrams. For the former, the potentials in the physical basis are

$$
\begin{aligned}
&V_{\bar{\mathrm{p}}\mathrm{p}\to\bar{\mathrm{p}}\mathrm{p}}^{\mathrm{PlanarBox}} = \\
&-\frac{5f_{NN\pi}^4}{8}\int\frac{\mathrm{d}^3\boldsymbol{l}_1}{(2\pi)^3}\frac{(\boldsymbol{l}_1^2-\boldsymbol{q}^2)^2\langle\lambda_2'|\lambda_2\rangle\langle\lambda_1'|\lambda_1\rangle-4\langle\lambda_2'|(\boldsymbol{l}_1\times\boldsymbol{q})\cdot\boldsymbol{\sigma}|\lambda_2\rangle\langle\lambda_1'|(\boldsymbol{l}_1\times\boldsymbol{q})\cdot\boldsymbol{\sigma}|\lambda_1\rangle}{\omega_{+,\pi}^2\omega_{-,\pi}^2(\omega_{+,\pi}+\omega_{-,\pi})} \\
&-\frac{f_{NN\pi}^2f_{NN\eta}^2}{4}\int\frac{\mathrm{d}^3\boldsymbol{l}_1}{(2\pi)^3}\frac{(\boldsymbol{l}_1^2-\boldsymbol{q}^2)^2\langle\lambda_2'|\lambda_2\rangle\langle\lambda_1'|\lambda_1\rangle-4\langle\lambda_2'|(\boldsymbol{l}_1\times\boldsymbol{q})\cdot\boldsymbol{\sigma}|\lambda_2\rangle\langle\lambda_1'|(\boldsymbol{l}_1\times\boldsymbol{q})\cdot\boldsymbol{\sigma}|\lambda_1\rangle}{\omega_{+,\eta}^2\omega_{-,\pi}^2(\omega_{+,\eta}+\omega_{-,\pi})} \\
&-\frac{f_{NN\eta}^4}{8}\int\frac{\mathrm{d}^3\boldsymbol{l}_1}{(2\pi)^3}\frac{(\boldsymbol{l}_1^2-\boldsymbol{q}^2)^2\langle\lambda_2'|\lambda_2\rangle\langle\lambda_1'|\lambda_1\rangle-4\langle\lambda_2'|(\boldsymbol{l}_1\times\boldsymbol{q})\cdot\boldsymbol{\sigma}|\lambda_2\rangle\langle\lambda_1'|(\boldsymbol{l}_1\times\boldsymbol{q})\cdot\boldsymbol{\sigma}|\lambda_1\rangle}{\omega_{+,\eta}^2\omega_{-,\eta}^2(\omega_{+,\eta}+\omega_{-,\eta})} \\
&-\frac{f_{\Lambda NK}^4}{8}\int\frac{\mathrm{d}^3\boldsymbol{l}_1}{(2\pi)^3}\frac{(\boldsymbol{l}_1^2-\boldsymbol{q}^2)^2\langle\lambda_2'|\lambda_2\rangle\langle\lambda_1'|\lambda_1\rangle-4\langle\lambda_2'|(\boldsymbol{l}_1\times\boldsymbol{q})\cdot\boldsymbol{\sigma}|\lambda_2\rangle\langle\lambda_1'|(\boldsymbol{l}_1\times\boldsymbol{q})\cdot\boldsymbol{\sigma}|\lambda_1\rangle}{\omega_{+,K}^2\omega_{-,K}^2(\omega_{+,K}+\omega_{-,K})} \\
&-\frac{5f_{\Sigma NK}^4}{8}\int\frac{\mathrm{d}^3\boldsymbol{l}_1}{(2\pi)^3}\frac{(\boldsymbol{l}_1^2-\boldsymbol{q}^2)^2\langle\lambda_2'|\lambda_2\rangle\langle\lambda_1'|\lambda_1\rangle-4\langle\lambda_2'|(\boldsymbol{l}_1\times\boldsymbol{q})\cdot\boldsymbol{\sigma}|\lambda_2\rangle\langle\lambda_1'|(\boldsymbol{l}_1\times\boldsymbol{q})\cdot\boldsymbol{\sigma}|\lambda_1\rangle}{\omega_{+,K}^2\omega_{-,K}^2(\omega_{+,K}+\omega_{-,K})} \\
&-\frac{f_{\Sigma NK}^2f_{\Lambda NK}^2}{4}\int\frac{\mathrm{d}^3\boldsymbol{l}_1}{(2\pi)^3}\frac{(\boldsymbol{l}_1^2-\boldsymbol{q}^2)^2\langle\lambda_2'|\lambda_2\rangle\langle\lambda_1'|\lambda_1\rangle-4\langle\lambda_2'|(\boldsymbol{l}_1\times\boldsymbol{q})\cdot\boldsymbol{\sigma}|\lambda_2\rangle\langle\lambda_1'|(\boldsymbol{l}_1\times\boldsymbol{q})\cdot\boldsymbol{\sigma}|\lambda_1\rangle}{\omega_{+,K}^2\omega_{-,K}^2(\omega_{+,K}+\omega_{-,K})}\,,
\end{aligned}
$$

$$
\begin{aligned}
&V_{\bar{\mathrm{p}}\mathrm{p}\to\bar{\mathrm{n}}\mathrm{n}}^{\mathrm{PlanarBox}} = \\
&-\frac{f_{NN\pi}^4}{2}\int\frac{\mathrm{d}^3\boldsymbol{l}_1}{(2\pi)^3}\frac{(\boldsymbol{l}_1^2-\boldsymbol{q}^2)^2\langle\lambda_2'|\lambda_2\rangle\langle\lambda_1'|\lambda_1\rangle-4\langle\lambda_2'|(\boldsymbol{l}_1\times\boldsymbol{q})\cdot\boldsymbol{\sigma}|\lambda_2\rangle\langle\lambda_1'|(\boldsymbol{l}_1\times\boldsymbol{q})\cdot\boldsymbol{\sigma}|\lambda_1\rangle}{\omega_{+,\pi}^2\omega_{-,\pi}^2(\omega_{+,\pi}+\omega_{-,\pi})} \\
&-\frac{f_{NN\pi}^2f_{NN\eta}^2}{2}\int\frac{\mathrm{d}^3\boldsymbol{l}_1}{(2\pi)^3}\frac{(\boldsymbol{l}_1^2-\boldsymbol{q}^2)^2\langle\lambda_2'|\lambda_2\rangle\langle\lambda_1'|\lambda_1\rangle-4\langle\lambda_2'|(\boldsymbol{l}_1\times\boldsymbol{q})\cdot\boldsymbol{\sigma}|\lambda_2\rangle\langle\lambda_1'|(\boldsymbol{l}_1\times\boldsymbol{q})\cdot\boldsymbol{\sigma}|\lambda_1\rangle}{\omega_{+,\eta}^2\omega_{-,\pi}^2(\omega_{+,\eta}+\omega_{-,\pi})} \\
&-\frac{f_{\Lambda NK}^4}{8}\int\frac{\mathrm{d}^3\boldsymbol{l}_1}{(2\pi)^3}\frac{(\boldsymbol{l}_1^2-\boldsymbol{q}^2)^2\langle\lambda_2'|\lambda_2\rangle\langle\lambda_1'|\lambda_1\rangle-4\langle\lambda_2'|(\boldsymbol{l}_1\times\boldsymbol{q})\cdot\boldsymbol{\sigma}|\lambda_2\rangle\langle\lambda_1'|(\boldsymbol{l}_1\times\boldsymbol{q})\cdot\boldsymbol{\sigma}|\lambda_1\rangle}{\omega_{+,K}^2\omega_{-,K}^2(\omega_{+,K}+\omega_{-,K})} \\
&-\frac{f_{\Sigma NK}^4}{8}\int\frac{\mathrm{d}^3\boldsymbol{l}_1}{(2\pi)^3}\frac{(\boldsymbol{l}_1^2-\boldsymbol{q}^2)^2\langle\lambda_2'|\lambda_2\rangle\langle\lambda_1'|\lambda_1\rangle-4\langle\lambda_2'|(\boldsymbol{l}_1\times\boldsymbol{q})\cdot\boldsymbol{\sigma}|\lambda_2\rangle\langle\lambda_1'|(\boldsymbol{l}_1\times\boldsymbol{q})\cdot\boldsymbol{\sigma}|\lambda_1\rangle}{\omega_{+,K}^2\omega_{-,K}^2(\omega_{+,K}+\omega_{-,K})} \\
&+\frac{f_{\Lambda NK}^2f_{\Sigma NK}^2}{4}\int\frac{\mathrm{d}^3\boldsymbol{l}_1}{(2\pi)^3}\frac{(\boldsymbol{l}_1^2-\boldsymbol{q}^2)^2\langle\lambda_2'|\lambda_2\rangle\langle\lambda_1'|\lambda_1\rangle-4\langle\lambda_2'|(\boldsymbol{l}_1\times\boldsymbol{q})\cdot\boldsymbol{\sigma}|\lambda_2\rangle\langle\lambda_1'|(\boldsymbol{l}_1\times\boldsymbol{q})\cdot\boldsymbol{\sigma}|\lambda_1\rangle}{\omega_{+,K}^2\omega_{-,K}^2(\omega_{+,K}+\omega_{-,K})}\,.
\end{aligned}
\tag{A.41}
$$

Transforming them into the isospin basis, one has

$$
\begin{aligned}
&V_{\bar{N}N}^{I=0} = \\
&-\frac{9f_{NN\pi}^4}{8}\int\frac{\mathrm{d}^3\boldsymbol{l}_1}{(2\pi)^3}\frac{(\boldsymbol{l}_1^2-\boldsymbol{q}^2)^2\langle\lambda_2'|\lambda_2\rangle\langle\lambda_1'|\lambda_1\rangle-4\langle\lambda_2'|(\boldsymbol{l}_1\times\boldsymbol{q})\cdot\boldsymbol{\sigma}|\lambda_2\rangle\langle\lambda_1'|(\boldsymbol{l}_1\times\boldsymbol{q})\cdot\boldsymbol{\sigma}|\lambda_1\rangle}{\omega_{+,\pi}^2\omega_{-,\pi}^2(\omega_{+,\pi}+\omega_{-,\pi})} \\
&-\frac{3f_{NN\pi}^2f_{NN\eta}^2}{4}\int\frac{\mathrm{d}^3\boldsymbol{l}_1}{(2\pi)^3}\frac{(\boldsymbol{l}_1^2-\boldsymbol{q}^2)^2\langle\lambda_2'|\lambda_2\rangle\langle\lambda_1'|\lambda_1\rangle-4\langle\lambda_2'|(\boldsymbol{l}_1\times\boldsymbol{q})\cdot\boldsymbol{\sigma}|\lambda_2\rangle\langle\lambda_1'|(\boldsymbol{l}_1\times\boldsymbol{q})\cdot\boldsymbol{\sigma}|\lambda_1\rangle}{\omega_{+,\eta}^2\omega_{-,\pi}^2(\omega_{+,\eta}+\omega_{-,\pi})} \\
&-\frac{f_{NN\eta}^4}{8}\int\frac{\mathrm{d}^3\boldsymbol{l}_1}{(2\pi)^3}\frac{(\boldsymbol{l}_1^2-\boldsymbol{q}^2)^2\langle\lambda_2'|\lambda_2\rangle\langle\lambda_1'|\lambda_1\rangle-4\langle\lambda_2'|(\boldsymbol{l}_1\times\boldsymbol{q})\cdot\boldsymbol{\sigma}|\lambda_2\rangle\langle\lambda_1'|(\boldsymbol{l}_1\times\boldsymbol{q})\cdot\boldsymbol{\sigma}|\lambda_1\rangle}{\omega_{+,\eta}^2\omega_{-,\eta}^2(\omega_{+,\eta}+\omega_{-,\eta})}
\end{aligned}
$$

JHEP08(2024)208

$$
-\frac{f_{\Lambda NK}^4}{4}\int\frac{\mathrm{d}^3\boldsymbol{l}_1}{(2\pi)^3}\frac{(\boldsymbol{l}_1^2-\boldsymbol{q}^2)^2\langle\lambda_2'|\lambda_2\rangle\langle\lambda_1'|\lambda_1\rangle-4\langle\lambda_2'|(\boldsymbol{l}_1\times\boldsymbol{q})\cdot\boldsymbol{\sigma}|\lambda_2\rangle\langle\lambda_1'|(\boldsymbol{l}_1\times\boldsymbol{q})\cdot\boldsymbol{\sigma}|\lambda_1\rangle}{\omega_{+,K}^2\omega_{-,K}^2(\omega_{+,K}+\omega_{-,K})}
$$

$$
-\frac{3f_{\Sigma NK}^4}{4}\int\frac{\mathrm{d}^3\boldsymbol{l}_1}{(2\pi)^3}\frac{(\boldsymbol{l}_1^2-\boldsymbol{q}^2)^2\langle\lambda_2'|\lambda_2\rangle\langle\lambda_1'|\lambda_1\rangle-4\langle\lambda_2'|(\boldsymbol{l}_1\times\boldsymbol{q})\cdot\boldsymbol{\sigma}|\lambda_2\rangle\langle\lambda_1'|(\boldsymbol{l}_1\times\boldsymbol{q})\cdot\boldsymbol{\sigma}|\lambda_1\rangle}{\omega_{+,K}^2\omega_{-,K}^2(\omega_{+,K}+\omega_{-,K})},
$$

$$
V_{\bar{N}N}^{I=1}=
$$

$$
-\frac{f_{NN\pi}^4}{8}\int\frac{\mathrm{d}^3\boldsymbol{l}_1}{(2\pi)^3}\frac{(\boldsymbol{l}_1^2-\boldsymbol{q}^2)^2\langle\lambda_2'|\lambda_2\rangle\langle\lambda_1'|\lambda_1\rangle-4\langle\lambda_2'|(\boldsymbol{l}_1\times\boldsymbol{q})\cdot\boldsymbol{\sigma}|\lambda_2\rangle\langle\lambda_1'|(\boldsymbol{l}_1\times\boldsymbol{q})\cdot\boldsymbol{\sigma}|\lambda_1\rangle}{\omega_{+,\pi}^2\omega_{-,\pi}^2(\omega_{+,\pi}+\omega_{-,\pi})}
$$

$$
+\frac{f_{NN\pi}^2f_{NN\eta}^2}{4}\int\frac{\mathrm{d}^3\boldsymbol{l}_1}{(2\pi)^3}\frac{(\boldsymbol{l}_1^2-\boldsymbol{q}^2)^2\langle\lambda_2'|\lambda_2\rangle\langle\lambda_1'|\lambda_1\rangle-4\langle\lambda_2'|(\boldsymbol{l}_1\times\boldsymbol{q})\cdot\boldsymbol{\sigma}|\lambda_2\rangle\langle\lambda_1'|(\boldsymbol{l}_1\times\boldsymbol{q})\cdot\boldsymbol{\sigma}|\lambda_1\rangle}{\omega_{+,\eta}^2\omega_{-,\pi}^2(\omega_{+,\eta}+\omega_{-,\pi})}
$$

$$
-\frac{f_{NN\eta}^4}{8}\int\frac{\mathrm{d}^3\boldsymbol{l}_1}{(2\pi)^3}\frac{(\boldsymbol{l}_1^2-\boldsymbol{q}^2)^2\langle\lambda_2'|\lambda_2\rangle\langle\lambda_1'|\lambda_1\rangle-4\langle\lambda_2'|(\boldsymbol{l}_1\times\boldsymbol{q})\cdot\boldsymbol{\sigma}|\lambda_2\rangle\langle\lambda_1'|(\boldsymbol{l}_1\times\boldsymbol{q})\cdot\boldsymbol{\sigma}|\lambda_1\rangle}{\omega_{+,\eta}^2\omega_{-,\eta}^2(\omega_{+,\eta}+\omega_{-,\eta})}
$$

$$
-\frac{f_{\Sigma NK}^4}{2}\int\frac{\mathrm{d}^3\boldsymbol{l}_1}{(2\pi)^3}\frac{(\boldsymbol{l}_1^2-\boldsymbol{q}^2)^2\langle\lambda_2'|\lambda_2\rangle\langle\lambda_1'|\lambda_1\rangle-4\langle\lambda_2'|(\boldsymbol{l}_1\times\boldsymbol{q})\cdot\boldsymbol{\sigma}|\lambda_2\rangle\langle\lambda_1'|(\boldsymbol{l}_1\times\boldsymbol{q})\cdot\boldsymbol{\sigma}|\lambda_1\rangle}{\omega_{+,K}^2\omega_{-,K}^2(\omega_{+,K}+\omega_{-,K})}
$$

$$
-\frac{f_{\Sigma NK}^2f_{\Lambda NK}^2}{2}\int\frac{\mathrm{d}^3\boldsymbol{l}_1}{(2\pi)^3}\frac{(\boldsymbol{l}_1^2-\boldsymbol{q}^2)^2\langle\lambda_2'|\lambda_2\rangle\langle\lambda_1'|\lambda_1\rangle-4\langle\lambda_2'|(\boldsymbol{l}_1\times\boldsymbol{q})\cdot\boldsymbol{\sigma}|\lambda_2\rangle\langle\lambda_1'|(\boldsymbol{l}_1\times\boldsymbol{q})\cdot\boldsymbol{\sigma}|\lambda_1\rangle}{\omega_{+,K}^2\omega_{-,K}^2(\omega_{+,K}+\omega_{-,K})}. \tag{A.42}
$$

For the crossed-box diagrams, the potentials are as follows

$$
\begin{aligned}
V_{\bar{\mathrm{p}}\mathrm{p}\to\bar{\mathrm{p}}\mathrm{p}}^{\mathrm{CrossBox}}=&-\frac{f_{NN\pi}^4}{8}\int\frac{\mathrm{d}^3\boldsymbol{l}_1}{(2\pi)^3}\frac{\omega_{+,\pi}^2+\omega_{-,\pi}\omega_{+,\pi}+\omega_{-,\pi}^2}{\omega_{-,\pi}^3\omega_{+,\pi}^3(\omega_{-,\pi}+\omega_{+,\pi})}[(\boldsymbol{l}_1^2-\boldsymbol{q}^2)^2\langle\lambda_2'|\lambda_2\rangle\langle\lambda_1'|\lambda_1\rangle\\
&+4\langle\lambda_2'|(\boldsymbol{l}_1\times\boldsymbol{q})\cdot\boldsymbol{\sigma}|\lambda_2\rangle\langle\lambda_1'|(\boldsymbol{l}_1\times\boldsymbol{q})\cdot\boldsymbol{\sigma}|\lambda_1\rangle]\\
&-\frac{f_{NN\pi}^2f_{NN\eta}^2}{4}\int\frac{\mathrm{d}^3\boldsymbol{l}_1}{(2\pi)^3}\frac{\omega_{+,\eta}^2+\omega_{-,\pi}\omega_{+,\eta}+\omega_{-,\pi}^2}{\omega_{-,\pi}^3\omega_{+,\eta}^3(\omega_{-,\pi}+\omega_{+,\eta})}[(\boldsymbol{l}_1^2-\boldsymbol{q}^2)^2\langle\lambda_2'|\lambda_2\rangle\langle\lambda_1'|\lambda_1\rangle\\
&+4\langle\lambda_2'|(\boldsymbol{l}_1\times\boldsymbol{q})\cdot\boldsymbol{\sigma}|\lambda_2\rangle\langle\lambda_1'|(\boldsymbol{l}_1\times\boldsymbol{q})\cdot\boldsymbol{\sigma}|\lambda_1\rangle]\\
&-\frac{f_{NN\eta}^4}{8}\int\frac{\mathrm{d}^3\boldsymbol{l}_1}{(2\pi)^3}\frac{\omega_{+,\eta}^2+\omega_{-,\eta}\omega_{+,\eta}+\omega_{-,\eta}^2}{\omega_{-,\eta}^3\omega_{+,\eta}^3(\omega_{-,\eta}+\omega_{+,\eta})}[(\boldsymbol{l}_1^2-\boldsymbol{q}^2)^2\langle\lambda_2'|\lambda_2\rangle\langle\lambda_1'|\lambda_1\rangle\\
&+4\langle\lambda_2'|(\boldsymbol{l}_1\times\boldsymbol{q})\cdot\boldsymbol{\sigma}|\lambda_2\rangle\langle\lambda_1'|(\boldsymbol{l}_1\times\boldsymbol{q})\cdot\boldsymbol{\sigma}|\lambda_1\rangle],
\end{aligned}
$$

$$
\begin{aligned}
V_{\bar{\mathrm{p}}\mathrm{p}\to\bar{\mathrm{n}}\mathrm{n}}^{\mathrm{CrossBox}}=&\frac{f_{NN\pi}^4}{2}\int\frac{\mathrm{d}^3\boldsymbol{l}_1}{(2\pi)^3}\frac{\omega_{+,\pi}^2+\omega_{-,\pi}\omega_{+,\pi}+\omega_{-,\pi}^2}{\omega_{-,\pi}^3\omega_{+,\pi}^3(\omega_{-,\pi}+\omega_{+,\pi})}[(\boldsymbol{l}_1^2-\boldsymbol{q}^2)^2\langle\lambda_2'|\lambda_2\rangle\langle\lambda_1'|\lambda_1\rangle\\
&+4\langle\lambda_2'|(\boldsymbol{l}_1\times\boldsymbol{q})\cdot\boldsymbol{\sigma}|\lambda_2\rangle\langle\lambda_1'|(\boldsymbol{l}_1\times\boldsymbol{q})\cdot\boldsymbol{\sigma}|\lambda_1\rangle]\\
&-\frac{f_{NN\pi}^2f_{NN\eta}^2}{2}\int\frac{\mathrm{d}^3\boldsymbol{l}_1}{(2\pi)^3}\frac{\omega_{+,\eta}^2+\omega_{-,\pi}\omega_{+,\eta}+\omega_{-,\pi}^2}{\omega_{-,\pi}^3\omega_{+,\eta}^3(\omega_{-,\pi}+\omega_{+,\eta})}[(\boldsymbol{l}_1^2-\boldsymbol{q}^2)^2\langle\lambda_2'|\lambda_2\rangle\langle\lambda_1'|\lambda_1\rangle\\
&+4\langle\lambda_2'|(\boldsymbol{l}_1\times\boldsymbol{q})\cdot\boldsymbol{\sigma}|\lambda_2\rangle\langle\lambda_1'|(\boldsymbol{l}_1\times\boldsymbol{q})\cdot\boldsymbol{\sigma}|\lambda_1\rangle].
\end{aligned} \tag{A.43}
$$

Transforming them into the isospin basis, one has

$$
\begin{aligned}
V_{\bar{N}N}^{I=0}=&\frac{3f_{NN\pi}^4}{8}\int\frac{\mathrm{d}^3\boldsymbol{l}_1}{(2\pi)^3}\frac{\omega_{+,\pi}^2+\omega_{-,\pi}\omega_{+,\pi}+\omega_{-,\pi}^2}{\omega_{-,\pi}^3\omega_{+,\pi}^3(\omega_{-,\pi}+\omega_{+,\pi})}[(\boldsymbol{l}_1^2-\boldsymbol{q}^2)^2\langle\lambda_2'|\lambda_2\rangle\langle\lambda_1'|\lambda_1\rangle\\
&+4\langle\lambda_2'|(\boldsymbol{l}_1\times\boldsymbol{q})\cdot\boldsymbol{\sigma}|\lambda_2\rangle\langle\lambda_1'|(\boldsymbol{l}_1\times\boldsymbol{q})\cdot\boldsymbol{\sigma}|\lambda_1\rangle]
\end{aligned}
$$

JHEP08(2024)208

$$
\begin{aligned}
&-\frac{3f_{NN\pi}^2 f_{NN\eta}^2}{4}\int\frac{\mathrm{d}^3\boldsymbol{l}_1}{(2\pi)^3}\frac{\omega_{+,\eta}^2+\omega_{-,\pi}\omega_{+,\eta}+\omega_{-,\pi}^2}{\omega_{-,\pi}^3\omega_{+,\eta}^3(\omega_{-,\pi}+\omega_{+,\eta})}[(\boldsymbol{l}_1^2-\boldsymbol{q}^2)^2\langle\lambda_2'|\lambda_2\rangle\langle\lambda_1'|\lambda_1\rangle\\
&+4\langle\lambda_2'|(\boldsymbol{l}_1\times\boldsymbol{q})\cdot\boldsymbol{\sigma}|\lambda_2\rangle\langle\lambda_1'|(\boldsymbol{l}_1\times\boldsymbol{q})\cdot\boldsymbol{\sigma}|\lambda_1\rangle]\\
&-\frac{f_{NN\eta}^4}{8}\int\frac{\mathrm{d}^3\boldsymbol{l}_1}{(2\pi)^3}\frac{\omega_{+,\eta}^2+\omega_{-,\eta}\omega_{+,\eta}+\omega_{-,\eta}^2}{\omega_{-,\eta}^3\omega_{+,\eta}^3(\omega_{-,\eta}+\omega_{+,\eta})}[(\boldsymbol{l}_1^2-\boldsymbol{q}^2)^2\langle\lambda_2'|\lambda_2\rangle\langle\lambda_1'|\lambda_1\rangle\\
&+4\langle\lambda_2'|(\boldsymbol{l}_1\times\boldsymbol{q})\cdot\boldsymbol{\sigma}|\lambda_2\rangle\langle\lambda_1'|(\boldsymbol{l}_1\times\boldsymbol{q})\cdot\boldsymbol{\sigma}|\lambda_1\rangle]\,,\\
V_{\bar{N}N}^{I=1}=&-\frac{5f_{NN\pi}^4}{8}\int\frac{\mathrm{d}^3\boldsymbol{l}_1}{(2\pi)^3}\frac{\omega_{+,\pi}^2+\omega_{-,\pi}\omega_{+,\pi}+\omega_{-,\pi}^2}{\omega_{-,\pi}^3\omega_{+,\pi}^3(\omega_{-,\pi}+\omega_{+,\pi})}[(\boldsymbol{l}_1^2-\boldsymbol{q}^2)^2\langle\lambda_2'|\lambda_2\rangle\langle\lambda_1'|\lambda_1\rangle\\
&+4\langle\lambda_2'|(\boldsymbol{l}_1\times\boldsymbol{q})\cdot\boldsymbol{\sigma}|\lambda_2\rangle\langle\lambda_1'|(\boldsymbol{l}_1\times\boldsymbol{q})\cdot\boldsymbol{\sigma}|\lambda_1\rangle]\\
&+\frac{f_{NN\pi}^2 f_{NN\eta}^2}{4}\int\frac{\mathrm{d}^3\boldsymbol{l}_1}{(2\pi)^3}\frac{\omega_{+,\eta}^2+\omega_{-,\pi}\omega_{+,\eta}+\omega_{-,\pi}^2}{\omega_{-,\pi}^3\omega_{+,\eta}^3(\omega_{-,\pi}+\omega_{+,\eta})}[(\boldsymbol{l}_1^2-\boldsymbol{q}^2)^2\langle\lambda_2'|\lambda_2\rangle\langle\lambda_1'|\lambda_1\rangle\\
&+4\langle\lambda_2'|(\boldsymbol{l}_1\times\boldsymbol{q})\cdot\boldsymbol{\sigma}|\lambda_2\rangle\langle\lambda_1'|(\boldsymbol{l}_1\times\boldsymbol{q})\cdot\boldsymbol{\sigma}|\lambda_1\rangle]\\
&-\frac{f_{NN\eta}^4}{8}\int\frac{\mathrm{d}^3\boldsymbol{l}_1}{(2\pi)^3}\frac{\omega_{+,\eta}^2+\omega_{-,\eta}\omega_{+,\eta}+\omega_{-,\eta}^2}{\omega_{-,\eta}^3\omega_{+,\eta}^3(\omega_{-,\eta}+\omega_{+,\eta})}[(\boldsymbol{l}_1^2-\boldsymbol{q}^2)^2\langle\lambda_2'|\lambda_2\rangle\langle\lambda_1'|\lambda_1\rangle\\
&+4\langle\lambda_2'|(\boldsymbol{l}_1\times\boldsymbol{q})\cdot\boldsymbol{\sigma}|\lambda_2\rangle\langle\lambda_1'|(\boldsymbol{l}_1\times\boldsymbol{q})\cdot\boldsymbol{\sigma}|\lambda_1\rangle]\,.
\end{aligned}
\tag{A.44}
$$

The isospin factors for planar-box and crossed-box diagrams are defined by

$$
\begin{aligned}
V_{\bar{N}N}^{\mathrm{PlanarBox}}=&-\mathcal{I}_{\bar{N}N\to\bar{N}N}^{\mathrm{PlanarBox}}\frac{f_{\bar{N}B_{i_1}P_1}^2 f_{\bar{N}B_{i_2}P_2}^2}{8}\times\\
&\int\frac{\mathrm{d}^3\boldsymbol{l}_1}{(2\pi)^3}\frac{(\boldsymbol{l}_1^2-\boldsymbol{q}^2)^2\langle\lambda_2'|\lambda_2\rangle\langle\lambda_1'|\lambda_1\rangle-4\langle\lambda_2'|(\boldsymbol{l}_1\times\boldsymbol{q})\cdot\boldsymbol{\sigma}|\lambda_2\rangle\langle\lambda_1'|(\boldsymbol{l}_1\times\boldsymbol{q})\cdot\boldsymbol{\sigma}|\lambda_1\rangle}{\omega_{+,P_1}^2\omega_{-,P_2}^2(\omega_{+,P_1}+\omega_{-,P_2})}\,,
\end{aligned}
$$

$$
\begin{aligned}
V_{\bar{N}N}^{\mathrm{CrossBox}}=&-\mathcal{I}_{\bar{N}N\to\bar{N}N}^{\mathrm{CrossBox}}\frac{f_{\bar{N}B_{i_1}P_1}^2 f_{\bar{N}B_{i_2}P_2}^2}{8}\int\frac{\mathrm{d}^3\boldsymbol{l}_1}{(2\pi)^3}\frac{\omega_{+,P_1}^2+\omega_{-,P_2}\omega_{+,P_1}+\omega_{-,P_2}^2}{\omega_{+,P_1}^3\omega_{-,P_2}^3(\omega_{+,P_1}+\omega_{-,P_2})}\times\\
&[(\boldsymbol{l}_1^2-\boldsymbol{q}^2)^2\langle\lambda_2'|\lambda_2\rangle\langle\lambda_1'|\lambda_1\rangle+4\langle\lambda_2'|(\boldsymbol{l}_1\times\boldsymbol{q})\cdot\boldsymbol{\sigma}|\lambda_2\rangle\langle\lambda_1'|(\boldsymbol{l}_1\times\boldsymbol{q})\cdot\boldsymbol{\sigma}|\lambda_1\rangle]\,.
\end{aligned}
\tag{A.45}
$$

The isospin factors are listed in table 5. In the next section, one can find the final expressions for these potentials, after the integration has been performed. Notice that the reducible parts of the box diagrams are not included to avoid double counting once the potential is resummed by the LS equation. See the first two graphs in the third row of figure 10.

B The integration of loop momentum

For TBE potentials, the integration over the loop momentum in the football, left and right triangle, planar and crossed-box diagrams needs to be dealt with [53]. For the football diagram, the potential in eq. (A.35) can be written as

$$
V_{\bar{N}N}^{\mathrm{Football}}=V_C^{\mathrm{Football}}\langle\lambda_2'|\lambda_2\rangle\langle\lambda_1'|\lambda_1\rangle\mathcal{I}_{\bar{N}N\to\bar{N}N}^{\mathrm{Football}}\,.
\tag{B.1}
$$

Here, after integration the potential V_C^{Football} has the following form

$$
V_C^{\mathrm{Football}}=\frac{1}{3072\pi^2 f_0^4}\left[-4m_P^2-\frac{5}{6}q^2+(6m_P^2+q^2)\left(\frac{R}{2}+\ln\frac{m_P}{\lambda}\right)+w^2(q)L(q)\right]\,,
\tag{B.2}
$$

JHEP08(2024)208

where we applied the renormalization scheme $\overline{\rm MS}-1$, and the divergent part is given as $R=\frac{2}{d-4}+\gamma_E-1-\ln(4\pi)$. The latter is ignored in the numerical calculation. λ is the renormalization scale introduced by dimensional regularization. It is absorbed into the contact terms. The subscript 'P' denotes the relevant pseudoscalar meson appearing in the intermediate states. The functions ω and L are given by

$$\begin{aligned} w(q;m_1,m_2) &= \frac{1}{q}\sqrt{(q^2+(m_1+m_2)^2)(q^2+(m_1-m_2)^2)}\,, \\ L(q;m_1,m_2) &= \frac{w(q)}{2q}\ln\frac{(qw(q)+q^2)^2-(m_1^2-m_2^2)^2}{4m_1m_2q^2}\,. \end{aligned} \tag{B.3}$$

For equal mass cases, they can be simplified as

$$\begin{aligned} w(q;m,m) &= \sqrt{q^2+4m^2}\,, \\ L(q;m,m) &= \frac{w(q)}{q}\ln\frac{w(q)+q}{2m} \end{aligned} \tag{B.4}$$

For the triangle diagrams, the potential in eq. (A.40) can be written as

$$V_{\bar{N}N}^{\rm Triangle} = f_{NB_iP}^2 V_C^{\rm Triangle}\langle\lambda_2'|\lambda_2\rangle\langle\lambda_1'|\lambda_1\rangle\mathcal{I}_{\bar{N}N\to\bar{N}N}^{\rm Triangle}\,, \tag{B.5}$$

where one has,

$$\begin{aligned} V_C^{\rm Triangle} = -\frac{1}{768\pi^2 f_0^2}\Bigg[&-4m_P^2-\frac{13}{3}q^2+(16m_P^2+10q^2)L(q) \\ &+(18m_P^2+5q^2)\left(R+2\ln\frac{m_P}{\lambda}\right)\Bigg]\,. \end{aligned} \tag{B.6}$$

For the planar box diagrams, the potential can be written as

$$\begin{aligned} V_{\bar{N}N}^{\rm PlanarBox} = f_{NB_{i_1}P_1}^2 f_{NB_{i_2}P_2}^2\Big(&V_C^{\rm PlanarBox}\langle\lambda_2'|\lambda_2\rangle\langle\lambda_1'|\lambda_1\rangle \\ &+V_S^{\rm PlanarBox}\langle\lambda_2'|\sigma_2^i|\lambda_2\rangle\langle\lambda_1'|\sigma_1^i|\lambda_1\rangle \\ &+V_T^{\rm PlanarBox}\langle\lambda_2'|\boldsymbol{\sigma}_2\cdot\boldsymbol{q}|\lambda_2\rangle\langle\lambda_1'|\boldsymbol{\sigma}_1\cdot\boldsymbol{q}|\lambda_1\rangle\Big)\mathcal{I}_{\bar{N}N\to\bar{N}N}^{\rm PlanarBox}\,, \end{aligned} \tag{B.7}$$

where one has

$$\begin{aligned} V_C^{\rm PlanarBox} = \frac{1}{192\pi^2}\Bigg[&\frac{5}{3}q^2+\frac{(m_{P_1}^2-m_{P_2}^2)^2}{q^2}+16(m_{P_1}^2+m_{P_2}^2) \\ &+(23q^2+45(m_{P_1}^2+m_{P_2}^2))\left(R+2\ln\frac{\sqrt{m_{P_1}m_{P_2}}}{\lambda}\right) \\ &+\frac{m_{P_1}^2-m_{P_2}^2}{q^4}(12q^4+(m_{P_1}^2-m_{P_2}^2)^2-9q^2(m_{P_1}^2+m_{P_2}^2))\ln\frac{m_{P_1}}{m_{P_2}} \\ &+\frac{2}{w^2(q)}\Bigg(23q^4-\frac{(m_{P_1}^2-m_{P_2}^2)^4}{q^4}+56(m_{P_1}^2+m_{P_2}^2)q^2 \\ &+8\frac{m_{P_1}^2+m_{P_2}^2}{q^2}(m_{P_1}^2-m_{P_2}^2)^2+2(21m_{P_1}^4+22m_{P_1}^2m_{P_2}^2+21m_{P_2}^4)\Bigg)L(q)\Bigg]\,, \end{aligned}$$

$$\begin{aligned} V_T^{\rm PlanarBox} &= -\frac{1}{8\pi^2}\left[L(q)-\frac{1}{2}-\frac{m_{P_1}^2-m_{P_2}^2}{2q^2}\ln\frac{m_{P_1}}{m_{P_2}}+\frac{R}{2}+\ln\frac{\sqrt{m_{P_1}m_{P_2}}}{\lambda}\right] \\ &= -\frac{1}{q^2}V_S^{\rm PlanarBox}\,, \end{aligned} \tag{B.8}$$

JHEP08(2024)208

where P_1 and P_2 denote the two exchanged pseudoscalar mesons. For the crossed-box diagrams, the potential can be written as

$$\begin{aligned} V_{\bar{N}N}^{\text{CrossBox}} = f_{NB_{i_1}P_1}^2 f_{NB_{i_2}P_2}^2 \Big(& V_C^{\text{CrossBox}} \langle \lambda_2' | \lambda_2 \rangle \langle \lambda_1' | \lambda_1 \rangle \\ & + V_S^{\text{CrossBox}} \langle \lambda_2' | \sigma_2^i | \lambda_2 \rangle \langle \lambda_1' | \sigma_1^i | \lambda_1 \rangle \\ & + V_T^{\text{CrossBox}} \langle \lambda_2' | \boldsymbol{\sigma}_2 \cdot \boldsymbol{q} | \lambda_2 \rangle \langle \lambda_1' | \boldsymbol{\sigma}_1 \cdot \boldsymbol{q} | \lambda_1 \rangle \Big) \mathcal{I}_{\bar{N}N \to \bar{N}N}^{\text{CrossBox}} , \end{aligned} \tag{B.9}$$

where one has

$$\begin{aligned} V_C^{\text{CrossBox}} &= -V_C^{\text{PlanarBox}} , \\ V_T^{\text{CrossBox}} &= -\frac{1}{q^2} V_S^{\text{CrossBox}} = V_T^{\text{PlanarBox}} . \end{aligned} \tag{B.10}$$

References

[1] A. Denig and G. Salme, *Nucleon Electromagnetic Form Factors in the Timelike Region*, *Prog. Part. Nucl. Phys.* **68** (2013) 113 [arXiv:1210.4689] [INSPIRE].

[2] L. Xia et al., *Proton Electromagnetic Form Factors in the Time-like Region through the Scan Technique*, *Symmetry* **14** (2022) 231 [arXiv:2111.13009] [INSPIRE].

[3] A. Bianconi and E. Tomasi-Gustafsson, *Periodic interference structures in the timelike proton form factor*, *Phys. Rev. Lett.* **114** (2015) 232301 [arXiv:1503.02140] [INSPIRE].

[4] E. Tomasi-Gustafsson, A. Bianconi and S. Pacetti, *New fit of timelike proton electromagnetic formfactors from e^+e^- colliders*, *Phys. Rev. C* **103** (2021) 035203 [arXiv:2012.14656] [INSPIRE].

[5] X. Cao, J.-P. Dai and H. Lenske, *Timelike nucleon electromagnetic form factors: All about interference of isospin amplitudes*, *Phys. Rev. D* **105** (2022) L071503 [arXiv:2109.15132] [INSPIRE].

[6] Y.-H. Lin, H.-W. Hammer and U.-G. Meißner, *New Insights into the Nucleon's Electromagnetic Structure*, *Phys. Rev. Lett.* **128** (2022) 052002 [arXiv:2109.12961] [INSPIRE].

[7] Y.-H. Lin, H.-W. Hammer and U.-G. Meißner, *Dispersion-theoretical analysis of the electromagnetic form factors of the nucleon: Past, present and future*, *Eur. Phys. J. A* **57** (2021) 255 [arXiv:2106.06357] [INSPIRE].

[8] R.-Q. Qian, Z.-W. Liu, X. Cao and X. Liu, *Toy model to understand the oscillatory behavior in timelike nucleon form factors*, *Phys. Rev. D* **107** (2023) L091502 [arXiv:2211.11555] [INSPIRE].

[9] E. Tomasi-Gustafsson and S. Pacetti, *Interpretation of recent form factor data in terms of an advanced representation of baryons in space and time*, *Phys. Rev. C* **106** (2022) 035203 [INSPIRE].

[10] Q.-H. Yang et al., *New insights into the oscillations of the nucleon electromagnetic form factors*, *Sci. Bull.* **68** (2023) 2729 [arXiv:2206.01494] [INSPIRE].

[11] C. Chen, B. Yan and J.-J. Xie, *Cross Sections and the Electromagnetic Form Factors within the Extended Vector Meson Dominance Model*, *Chin. Phys. Lett.* **41** (2024) 021302 [arXiv:2312.16753] [INSPIRE].

JHEP08(2024)208

[12] F. Rosini, S. Pacetti, O. Shekhovtsova and E. Tomasi-Gustafsson, *Microscopic parametrization of the near threshold oscillations of the nucleon time-like effective electromagnetic form factors*, *Eur. Phys. J. A* **60** (2024) 144 [arXiv:2403.02916] [INSPIRE].

[13] M. Castellano et al., *The reaction $e^+e^- \to p\bar{p}$ at a total energy of 2.1 gev*, *Nuovo Cim. A* **14** (1973) 1 [INSPIRE].

[14] B. Delcourt et al., *Study of the Reaction $e^+e^- \to p\bar{p}$ in the Total Energy Range* 1925 *MeV* – 2180 *MeV*, *Phys. Lett. B* **86** (1979) 395 [INSPIRE].

[15] D. Bisello et al., *>A Measurement of $e^+e^- \to \bar{p}p$ for* 1975 *MeV* $\leq \sqrt{s} \leq$ 2250 *MeV*, *Nucl. Phys. B* **224** (1983) 379 [INSPIRE].

[16] DM2 collaboration, *Baryon pair production in e^+e^- annihilation at $\sqrt{s} = 2.4$ GeV*, *Z. Phys. C* **48** (1990) 23 [INSPIRE].

[17] A. Antonelli et al., *First measurement of the neutron electromagnetic form-factor in the timelike region*, *Phys. Lett. B* **313** (1993) 283 [INSPIRE].

[18] A. Antonelli et al., *Measurement of the electromagnetic form-factor of the proton in the timelike region*, *Phys. Lett. B* **334** (1994) 431 [INSPIRE].

[19] A. Antonelli et al., *The first measurement of the neutron electromagnetic form-factors in the timelike region*, *Nucl. Phys. B* **517** (1998) 3 [INSPIRE].

[20] Mulhouse-Strasbourg-Turin collaboration, *First Determination of the Proton Electromagnetic Form-Factors at the Threshold of the Timelike Region*, *Phys. Lett. B* **68** (1977) 477 [INSPIRE].

[21] BaBar collaboration, *A study of $e^+e^- \to p\bar{p}$ using initial state radiation with BABAR*, *Phys. Rev. D* **73** (2006) 012005 [hep-ex/0512023] [INSPIRE].

[22] BaBar collaboration, *Study of $e^+e^- \to p\bar{p}$ via initial-state radiation at BABAR*, *Phys. Rev. D* **87** (2013) 092005 [arXiv:1302.0055] [INSPIRE].

[23] CMD-3 collaboration, *Study of the process $e^+e^- \to p\bar{p}$ in the c.m. energy range from threshold to 2 GeV with the CMD-3 detector*, *Phys. Lett. B* **759** (2016) 634 [arXiv:1507.08013] [INSPIRE].

[24] CMD-3 collaboration, *Observation of a fine structure in $e^+e^- \to$ hadrons production at the nucleon-antinucleon threshold*, *Phys. Lett. B* **794** (2019) 64 [arXiv:1808.00145] [INSPIRE].

[25] BES collaboration, *Measurement of the cross section for $e^+e^- \to p\bar{p}$ at center-of-mass energies from 2.0-GeV to 3.07-GeV*, *Phys. Lett. B* **630** (2005) 14 [hep-ex/0506059] [INSPIRE].

[26] BESIII collaboration, *Measurement of the proton form factor by studying $e^+e^- \to p\bar{p}$*, *Phys. Rev. D* **91** (2015) 112004 [arXiv:1504.02680] [INSPIRE].

[27] BESIII collaboration, *Study of the process $e^+e^- \to p\bar{p}$ via initial state radiation at BESIII*, *Phys. Rev. D* **99** (2019) 092002 [arXiv:1902.00665] [INSPIRE].

[28] BESIII collaboration, *Measurement of proton electromagnetic form factors in $e^+e^- \to p\bar{p}$ in the energy region* 2.00–3.08 *GeV*, *Phys. Rev. Lett.* **124** (2020) 042001 [arXiv:1905.09001] [INSPIRE].

[29] BESIII collaboration, *Measurement of proton electromagnetic form factors in the time-like region using initial state radiation at BESIII*, *Phys. Lett. B* **817** (2021) 136328 [arXiv:2102.10337] [INSPIRE].

[30] M.N. Achasov et al., *Study of the process $e^+e^- \to n\bar{n}$ at the VEPP-2000 e^+e^- collider with the SND detector*, *Phys. Rev. D* **90** (2014) 112007 [arXiv:1410.3188] [INSPIRE].

JHEP08(2024)208

[31] V.P. Druzhinin and S.I. Serednyakov, *Measurement of the $e^+e^- \to n\bar{n}$ cross section with the SND detector at the VEPP-2000 collider*, *EPJ Web Conf.* **212** (2019) 07007 [INSPIRE].

[32] BESIII collaboration, *Oscillating features in the electromagnetic structure of the neutron*, *Nature Phys.* **17** (2021) 1200 [arXiv:2103.12486] [INSPIRE].

[33] SND collaboration, *Experimental study of the $e^+e^- \to n\bar{n}$ process at the VEPP-2000 e^+e^- collider with the SND detector*, *Eur. Phys. J. C* **82** (2022) 761 [arXiv:2206.13047] [INSPIRE].

[34] BESIII collaboration, *Measurements of the Electric and Magnetic Form Factors of the Neutron for Timelike Momentum Transfer*, *Phys. Rev. Lett.* **130** (2023) 151905 [arXiv:2212.07071] [INSPIRE].

[35] L.-Y. Dai and M.R. Pennington, *Comprehensive amplitude analysis of $\gamma\gamma \to \pi^+\pi^-, \pi^0\pi^0$ and $\overline{K}K$ below 1.5 GeV*, *Phys. Rev. D* **90** (2014) 036004 [arXiv:1404.7524] [INSPIRE].

[36] D.-L. Yao, L.-Y. Dai, H.-Q. Zheng and Z.-Y. Zhou, *A review on partial-wave dynamics with chiral effective field theory and dispersion relation*, *Rept. Prog. Phys.* **84** (2021) 076201 [arXiv:2009.13495] [INSPIRE].

[37] S.-J. Wang, Z. Fang and L.-Y. Dai, *Two body final states production in electron-positron annihilation and their contributions to $(g-2)_\mu$*, *JHEP* **07** (2023) 037 [arXiv:2302.08859] [INSPIRE].

[38] E. Epelbaum, W. Glöckle and U.-G. Meißner, *The Two-nucleon system at next-to-next-to-next-to-leading order*, *Nucl. Phys. A* **747** (2005) 362 [nucl-th/0405048] [INSPIRE].

[39] R. Machleidt and D.R. Entem, *Chiral effective field theory and nuclear forces*, *Phys. Rept.* **503** (2011) 1 [arXiv:1105.2919] [INSPIRE].

[40] J. Haidenbauer, X.-W. Kang and U.-G. Meißner, *The electromagnetic form factors of the proton in the timelike region*, *Nucl. Phys. A* **929** (2014) 102 [arXiv:1405.1628] [INSPIRE].

[41] L.-Y. Dai, J. Haidenbauer and U.G. Meißner, *Re-examining the $X(4630)$ resonance in the reaction $e^+e^- \to \Lambda_c^+\bar{\Lambda}_c^-$*, *Phys. Rev. D* **96** (2017) 116001 [arXiv:1710.03142] [INSPIRE].

[42] J. Haidenbauer, U.-G. Meißner and L.-Y. Dai, *Hyperon electromagnetic form factors in the timelike region*, *Phys. Rev. D* **103** (2021) 014028 [arXiv:2011.06857] [INSPIRE].

[43] Q.-H. Yang, D. Guo and L.-Y. Dai, *Structure around $p\bar{p}$ threshold in J/ψ radiative decays*, *Phys. Rev. D* **107** (2023) 034030 [arXiv:2209.10101] [INSPIRE].

[44] J. Haidenbauer and U.G. Meißner, *The electromagnetic form factors of the Λ in the timelike region*, *Phys. Lett. B* **761** (2016) 456 [arXiv:1608.02766] [INSPIRE].

[45] X. Cao, J.-P. Dai and Y.-P. Xie, *Vector mesons and electromagnetic form factor of the Λ hyperon*, *Phys. Rev. D* **98** (2018) 094006 [arXiv:1808.06382] [INSPIRE].

[46] B. Yan, C. Chen and J.-J. Xie, *Σ and Ξ electromagnetic form factors in the extended vector meson dominance model*, *Phys. Rev. D* **107** (2023) 076008 [arXiv:2301.00976] [INSPIRE].

[47] A.D. Martin and T.D. Spearman, *Elementary Partical Theory*, North-Holland Publishing, The Netherlands (1970) [ISBN: 9780720401578].

[48] S.-Q. Kuang et al., *Study of X(6900) with unitarized coupled channel scattering amplitudes*, *Eur. Phys. J. C* **83** (2023) 383 [arXiv:2302.03968] [INSPIRE].

[49] N.H. Buttimore and E. Jennings, *Polarisation observables in lepton antilepton to proton antiproton reactions including lepton mass*, *Eur. Phys. J. A* **31** (2007) 9 [hep-ph/0607227] [INSPIRE].

JHEP08(2024)208

[50] N.H. Buttimore and E. Jennings, *Helicity amplitudes and crossing relations for antiproton proton reactions*, *Eur. Phys. J. A* **33** (2007) 21 [hep-ph/0702248] [INSPIRE].

[51] E. Epelbaum, H. Krebs and U.-G. Meißner, *Improved chiral nucleon-nucleon potential up to next-to-next-to-next-to-leading order*, *Eur. Phys. J. A* **51** (2015) 53 [arXiv:1412.0142] [INSPIRE].

[52] E. Epelbaum, W. Gloeckle and U.-G. Meißner, *Nuclear forces from chiral Lagrangians using the method of unitary transformation. I. Formalism*, *Nucl. Phys. A* **637** (1998) 107 [nucl-th/9801064] [INSPIRE].

[53] E. Epelbaum, W. Gloeckle and U.-G. Meissner, *Nuclear forces from chiral Lagrangians using the method of unitary transformation. II. The two nucleon system*, *Nucl. Phys. A* **671** (2000) 295 [nucl-th/9910064] [INSPIRE].

[54] J. Haidenbauer et al., *Hyperon-nucleon interaction at next-to-leading order in chiral effective field theory*, *Nucl. Phys. A* **915** (2013) 24 [arXiv:1304.5339] [INSPIRE].

[55] S. Petschauer et al., *Hyperon-nuclear interactions from SU(3) chiral effective field theory*, *Front. in Phys.* **8** (2020) 12 [arXiv:2002.00424] [INSPIRE].

[56] J. Haidenbauer and U.-G. Meißner, *Predictions for the strangeness $S = -3$ and -4 baryon-baryon interactions in chiral effective field theory*, *Phys. Lett. B* **684** (2010) 275 [arXiv:0907.1395] [INSPIRE].

[57] J. Haidenbauer, U.-G. Meißner and S. Petschauer, *Strangeness $S = -2$ baryon-baryon interaction at next-to-leading order in chiral effective field theory*, *Nucl. Phys. A* **954** (2016) 273 [arXiv:1511.05859] [INSPIRE].

[58] J. Haidenbauer, U.-G. Meißner, A. Nogga and H. Le, *Hyperon-nucleon interaction in chiral effective field theory at next-to-next-to-leading order*, *Eur. Phys. J. A* **59** (2023) 63 [arXiv:2301.00722] [INSPIRE].

[59] X.-W. Kang, J. Haidenbauer and U.-G. Meißner, *Antinucleon-nucleon interaction in chiral effective field theory*, *JHEP* **02** (2014) 113 [arXiv:1311.1658] [INSPIRE].

[60] L.-Y. Dai, J. Haidenbauer and U.-G. Meißner, *$J/\psi \to \gamma\eta'\pi^+\pi^-$ and the structure observed around the $\bar{p}p$ threshold*, *Phys. Rev. D* **98** (2018) 014005 [arXiv:1804.07077] [INSPIRE].

[61] L.-Y. Dai, J. Haidenbauer and U.-G. Meißner, *Antinucleon-nucleon interaction at next-to-next-to-next-to-leading order in chiral effective field theory*, *JHEP* **07** (2017) 078 [arXiv:1702.02065] [INSPIRE].

[62] D. Zhou and R.G.E. Timmermans, *Energy-dependent partial-wave analysis of all antiproton-proton scattering data below 925 MeV/c*, *Phys. Rev. C* **86** (2012) 044003 [arXiv:1210.7074] [INSPIRE].

[63] G. Bardin et al., *Determination of the electric and magnetic form-factors of the proton in the timelike region*, *Nucl. Phys. B* **411** (1994) 3 [INSPIRE].

[64] D. Guo, Q.-H. Yang and L.-Y. Dai, *Study of the timelike electromagnetic form factors of the Λc*, *Phys. Rev. D* **109** (2024) 114005 [arXiv:2404.06191] [INSPIRE].

[65] V. Bernard, N. Kaiser and U.-G. Meißner, *Chiral dynamics in nucleons and nuclei*, *Int. J. Mod. Phys. E* **4** (1995) 193 [hep-ph/9501384] [INSPIRE].

[66] R. Machleidt, K. Holinde and C. Elster, *The Bonn Meson Exchange Model for the Nucleon Nucleon Interaction*, *Phys. Rept.* **149** (1987) 1 [INSPIRE].

JHEP08(2024)208